Efficiency and adaptability of the benthic methane filter at Quepos Slide cold seeps, offshore Costa Rica

Philip Steeb[1]*, Stefan Krause[1], Peter Linke[1], Christian Hensen[1], Andrew W. Dale[1], Marianne Nuzzo[2], Tina Treude[13]*

[1]GEOMAR Helmholtz Centre for Ocean Research Kiel, Wischhofstrasse 1-3, D- 24148 Kiel, Germany

[2]LNEG, Marine Geology Department, Alfragide, Portugal & Institute Dom Luiz, University of Lisbon, Lisbon, Portugal. Now at Integrated Geochemical Interpretation, Ltd. (UK)

[3]Present address: University of California, Los Angeles, Department of Earth Planetary & Space Sciences and Department of Atmospheric and Oceanic Sciences, Los Angeles, CA, USA

*Corresponding Authors: psteeb@geomar.de, ttreude@g.ucla.edu

Working Title: Quepos Slide SLOT System

Abstract:

Large amounts of methane are delivered by fluids through the erosive forearc of the convergent margin offshore Costa Rica and lead to the formation of cold seeps at the sediment surface. Besides mud extrusion, numerous cold seeps are created by landslides induced by seamount subduction or fluid migration along major faults. Most of the dissolved methane migrating through the sediments of cold seeps is oxidized within the benthic microbial methane filter by anaerobic oxidation of methane (AOM). Measurements of AOM and sulfate reduction as well as numerical modeling of porewater profiles revealed a highly active and efficient benthic methane filter at Quepos Slide site; a landslide on the continental slope between the Nicoya and Osa Peninsula. Integrated areal rates of AOM ranged from 12.9 ± 6.0 to 45.2 ± 11.5 mmol m^{-2} d^{-1} , with only 1 to 2.5% of the upward methane flux being released into the water column.

Additionally, two parallel sediment cores from Quepos Slide were used for in vitro experiments in a recently developed Sediment-Flow-Through (SLOT) system to simulate an increased fluid and methane flux from the bottom of the sediment core. The benthic methane filter revealed a high adaptability whereby the methane oxidation efficiency responded to the increased fluid flow within

ca. 170 d. To our knowledge, this study provides the first estimation of the natural biogeochemical response of seep sediments to changes in fluid flow.

1. Introduction:

Subduction zones represent large-scale systems of sediment and element recycling. Organic carbon accumulation at continental margins can lead to the formation of large methane reservoirs through its biological or thermogenic breakdown (Judd et al. 2002; Schmidt et al. 2005; Hensen and Wallmann 2005; Crutchley et al. 2014). Produced methane gas may be transported upwards in solution by molecular diffusion or by ascending fluids, mobilized by, e.g., sediment compaction or clay mineral dehydration (Hensen et al. 2004; Tryon et al. 2010; Crutchley et al. 2014). When the fluids are highly enriched in hydrocarbon gases, gas hydrates may precipitate depending on the pressure-temperature conditions (Hensen and Wallmann 2005). Gas hydrates sometimes block fluid pathways (Tryon et al. 2002; Minami et al. 2012) and change the composition of fluids flowing through the gas hydrate stability zone (GHSZ). Alternatively, dissociating gas hydrates can act as additional sources for methane and fluids (Kvenvolden 2002), or dilute fluids when they dissolve (Hesse et al. 2000; Hensen et al. 2004).

The migration of methane-charged fluids towards the sediment-water interface creates so called "cold seeps" (Judd et al. 2002; Suess 2010). Within the surface sediment, the majority of the methane is consumed by the anaerobic oxidation of methane (AOM) (Hinrichs and Boetius 2002; Knittel and Boetius 2009). AOM is coupled to sulfate reduction and produces dissolved bicarbonate and sulfide. The reaction is mediated by a consortia of anaerobic methanotrophic (ANME) archaea and sulfate-reducing bacteria (SRB) (Boetius et al. 2000). Recent studies propose that some ANME can reduce sulfate without the aid of SRB (Milucka et al. 2012). Additionally, the use of other electron acceptors such as Mn, Fe (Beal et al. 2009), or nitrate (Ettwig et al. 2010) is also possible. However, sulfate is the most abundant electron acceptor in seawater and AOM coupled to sulfate reduction is,

52 to our knowledge, the by far most important anaerobic pathway for methane oxidation in marine
53 settings (Reeburgh 2007).
54 The sediment zone, in which methane and sulfate concentrations overlap, is termed the sulfate-
55 methane transition zone (SMTZ). The depth of the SMTZ is dependent on (1) sulfate depletion
56 resulting from organic matter degradation (Borowski et al. 1999), (2) sulfate supply by diffusion,
57 bioirrigation and sulfide re-oxidation reactions (Dale et al. 2009), (3) the flux of methane from below
58 the SMTZ (Borowski et al. 1996), and (4) the advective fluid flow rate (Treude et al. 2003; Orcutt et al.
59 2011). At continental margins, the SMTZ can sometimes be located several hundreds of meters
60 below the seafloor (mbsf) (Borowski et al. 1999). In coastal sediments, sulfate is consumed rapidly via
61 organoclastic sulfate reduction fueled by an enhanced supply of organic matter and, subsequently,
62 the SMTZ is often located closer to the sediment-water interface compared to sediments in greater
63 water depths (Hinrichs and Boetius 2002). At seepage sites, upwards advective flow of methane-rich
64 fluid pushes the SMTZ closer to the surface, occasionally to only a few centimeters below the
65 seafloor (cmbsf) (Treude et al. 2003; Niemann et al. 2006; Krause et al. 2014). At the center of the
66 Håkon Mosby Mud Volcano, advective fluid flow is so high that it inhibits sulfate penetration into the
67 sediment (de Beer et al. 2006; Niemann et al. 2006), resulting in the absence of a SMTZ. The depth of
68 the SMTZ determines, which chemolithotrophic seep organisms have access to the produced sulfide.
69 The prevailing communities serve as indicators of seepage intensity. Sites covered by mats of sulfur
70 bacteria (e.g. *Beggiatoa*) exhibit a very shallow SMTZ (few cm) compared to clam sites (e.g.
71 *Calyptogena*) with SMTZ depth of ~5-10 cm, or even deeper SMTZ in tubeworm or *Solemya* habitats
72 (Sahling et al. 2002; Levin 2003; Treude et al. 2003; Mau et al. 2006; Fischer et al. 2012).
73 In the present study, we compared data from field measurements, numerical modeling, and
74 laboratory flow-through experiments of samples taken at Quepos Slide, a submarine landslide on the
75 Pacific coast off Costa Rica (Bohrmann et al. 2002; Karaca et al. 2012), to investigate the effect of
76 fluid flow on methane consumption and emission. The numerical model was developed to compare
77 with direct measurements of AOM and sulfate reduction rates and to determine the magnitude of

78 the fluid advection velocity. In laboratory experiments, undisturbed sediments from Quepos Slide
79 were exposed to different flow conditions, to investigate the development of the SMTZ and the
80 response of the benthic microbial methane filter. For this objective, we used a newly developed
81 Sediment-Flow-Through system, referred to as SLOT (Steeb et al. 2014), which mimics natural fluid-
82 flow regimes. It was the overall goal of this study to better understand mechanisms controlling the
83 efficiency of this methane filter, which plays a major role in reducing greenhouse gas emissions from
84 the ocean into the atmosphere (Reeburgh 2007).
85
86 **1.2 Geological Setting:** At the Mid-American Trench, the Cocos Plate in the north and Nazca Plate in
87 the south are subducted below the Caribbean Plate at a velocity of 8.8 cm yr^{-1} (Syracuse and Abers
88 2006). Here, seep features like mud volcanoes, mud diapirs, and pockmarks are very abundant. More
89 than 100 seeps localities have been identified at the central Costa Rican Pacific Trench, on average
90 one seep every 4 km (Sahling et al. 2008). Recent high-resolution mapping revealed even greater
91 seep density in this region (Kluesner et al. 2013). Between the Nicoya (north) and Osa Peninsula
92 (south), seamounts from the Nasca Plate are subducted (Ranero and von Huene 2000), resulting in
93 slope failures and landslides or scarps (e. g., Jaco Scarp, BGR landslide, GEOMAR landslide; Harders et
94 al. 2011; Ranero et al. 2008). Landslide-induced seeps are created by opening new structural and
95 stratigraphical fluid pathways (Ranero et al. 2008; Mau et al. 2012) or by gas hydrate dissociation
96 resulting from altered pressure and temperature conditions.
97 Fluids and related methane fluxes can vary both spatially and temporally as well as in origin,
98 composition, and flow velocity. Temporal variations can be caused by gas hydrate formation and
99 dissociation (Hesse et al. 2000; Tryon et al. 2002; Hensen et al. 2004; Minami et al. 2012) or triggered
100 by earthquakes, which are frequent in this active subduction zone (Tryon et al. 2002; Hensen et al.
101 2004; Aiello 2005; Henrys et al. 2006; Mau et al. 2007; Fischer et al. 2013).
102 Well-known examples exhibiting such dynamics are the twin mounds “Mound 11” and “Mound 12”,
103 located at 1000 m water depth, halfway between the Nicoya and Osa Peninsulas. Both mounds are

104 located at the same fault zone, although they differ in fluid flow advection intensity (Hensen et al.
105 2004; Linke et al. 2005; Karaca et al. 2010; Krause et al. 2014), fluid origin (Hensen et al. 2004; Han et
106 al. 2004; Schmidt et al. 2005), and microbial activity (Krause et al. 2014). In the last 50 kyr both
107 mounds have displayed individual active phases interrupted by phases of inactivity (Kutterolf et al.
108 2008). In contrast to this long term variability, Füri et al. (2010) observed a two month seepage event
109 at Mound 11 with flow rates that varied four-fold (from 5 cm yr^{-1} to 20 cm yr^{-1}). Events like this affect
110 the efficiency of the benthic microbial methane filter and result in increased methane concentrations
111 in the water column. Slow adaptation to increased methane supply may explain elevated methane
112 concentrations in the water column offshore Costa Rica found by Mau et al. (2007) in 2003,
113 presumably caused by an earthquake earlier that year.
114 The research area of the present study, the Quepos Slide, is located south of the twin Mounds 11 and
115 12. This landslide is approximately 9.5 km wide and 8 km long (Harders 2011). The translational slide
116 has a headwall 160 m in height and the slide head is located at ~400 m water depth in the Eastern
117 Pacific oxygen minimum zone (OMZ; between 250 -550 m water depth; Bohrmann et al. 2002). Four
118 tongues of the landslide can be identified, reaching down to ~800 water depth, indicating three
119 subsequent events following the initial slide (Bohrmann et al. 2002; Harders et al. 2011). The Quepos
120 Slide was most likely caused by seamount subduction (Harders et al. 2011). Along the toe, fluids and
121 gas can migrate from hydrates inside the GHSZ. Chemosynthetic organisms are abundant, with
122 bacterial mats present throughout, while authigenic carbonates and clams can be found at deeper
123 areas and at the toe of the slide (Bohrmann et al. 2002). Directly below the headwall, the sediments
124 are covered by sulfur bacteria mats (Bohrmann et al. 2002; Sahling et al. 2008; Karaca et al. 2012).
125 Empirical models show that vertical fluid flow at Quepos Slide varies between 1 and 40 cm yr^{-1} and
126 AOM rates vary between 1.5 and 42.1 mmol m^{-2} d^{-1} (Karaca et al. 2012). According to that model,
127 53% (~316 x 10^3 mol yr^{-1}) of the methane is oxidized by the highly active benthic microbial methane
128 filter, while 47% (280 x 10^3 mol yr^{-1}) is released into the water column. Elevated methane

129 concentrations of 72 nmol l^{-1} was observed in the seawater directly above the slide head (Bohrmann

130 et al. 2002).

2. Methods:

Surface sediments from Quepos Slide were obtained by a video-guided multi-corer (TV-MUC) during the GEOMAR research cruise SO206 in June 2010 on the German research vessel "SONNE". Two sites (SO206-29 MUC, SO206-31 MUC) from the headwall of Quepos Slide, both covered by sulfur bacteria mats, were sampled (Table 1). All subsampling procedures were performed on board at 4°C immediately after obtaining the sediments. Three replicate cores (inner diameter 10 cm) of each TV-MUC were used for (1) porewater analyses, (2) ex situ AOM and sulfate reduction rate assays, and (3) methane concentration determination. Additionally, two replicate cores of SO206-31 (MUC) were sub-sampled for laboratory experiments (SLOT-system, see below).

2.1 Porewater measurement (ex situ): Porewater of the ex situ samples was extracted by a pressure-filtration system and filtered (argon 3–4 bar, 0.2 µm regenerated cellulose filters, Krause et al. 2014). Total alkalinity (TA) was analyzed onboard via titration (Ivanenkov and Lyakhin 1978). Sulfide was determined photometrically using the methylene blue method (Cline 1969). Sub-samples for the determination of sulfate, chloride, and bromide were frozen and analyzed onshore by ion chromatography (Compact IC 761). Further porewater sampling and analytical procedures are described in detail by Krause et al. (2013).

2.2 Methane (ex situ): For methane determination, 10 cm^3 of sediment was transferred to 30 mL glass vials filled with 10 ml 10% KCl for poisoning and headspace equilibration. The methane concentration was determined on board by gas chromatography coupled to a flame ionization detector (GC-FID) using a Shimadzu GC14A instrument fitted with a Restek Rt®Alumina Bond/KCl capillary column (50 m, 0.53 mm ID) operated at 60 C. N2 was used as a carrier gas.

2.3 Microbial rate measurement (ex situ): Ex situ turnover rates of sulfate reduction and AOM were determined with radiotracer techniques. For both sulfate reduction and AOM, three replicate polycarbonate tubes (26 mm inner diameter, 250 mm length) were sub-sampled from one TV-MUC core and incubated by whole core incubation (Jørgensen 1978). Additional bulk sediment was sampled to produce controls. Fifteen µl $^{14}CH_4$ (1–2 kBq dissolved in anoxic, sterile water; specific

activity 22.28 GBq $mmol^{-1}$), and 6 µl $^{35}SO_4^{2-}$ (200 kBq dissolved in water; specific activity 37 TBq $mmol^{-1}$), was injected into the AOM and sulfate reduction cores, respectively, at a vertical resolution of 1 cm; the cores were then incubated for 24 h in the dark at in situ temperature (8°C). After incubation, the sediment cores were sliced in 1 cm intervals and transferred to 20 ml NaOH (2.5% w/v, 40 ml glas vials with rubber stopper) for AOM, and 20 ml zinc acetate (20% w/v, 50 ml plastic vials) for sulfate reduction determinations. Control samples (five each), were first transferred to the respective chemicals before tracer was added (see above). AOM was determined according to Treude et al. (2005)(GC and Combustion) and Joye et al. (2004) ($^{14}CO_2$ trapping). Sulfate reduction was determined using the cold chromium distillation method after Kallmeyer et al. (2004).

2.4 Numerical model: Porewater profiles were simulated using a one-dimensional transport reaction model, previously used and described by Krause et al. (2013), to determine the flow velocity of the fluid and the rate of AOM. Carbonate precipitation was implemented in the model (Krause et al., 2013) but was not used in the present study for simplicity, since carbonate precipitation does not affect the efficiency of the microbial benthic methane filter within the studied time scales (several months to years). Because the sampling sites were located above the GHSZ (Wallmann et al. 2012), dissolved methane concentrations at the lower boundary were calculated from the equilibrium concentration with free gas (Tishchenko et al. 2005). Table 2 provides an overview of other boundary conditions as well as fitted, measured, and calculated parameters of the model.

2.5 Sediment-Flow-Through System: The response of the sediment to changes in fluid and methane fluxes was studied using a newly-developed Sediment-Flow-Through (SLOT)-system (Steeb et al. 2014), which mimics natural flow conditions with diffusive supply of sulfate at the sediment surface and advective methane supply at the bottom of the core. The system enables continuous monitoring of geochemical gradients inside the sediment as well as in the in- and outflow and allows the development of the geochemical gradients and SMTZ to be observed. The efficiency of the benthic microbial methane filter during the transient periods can be calculated from the measured input and output fluxes (see below). For the present study we focused only on AOM, i.e., all incubations were

kept strictly anoxic, as AOM is the most important process for methane removal in the sediment. The system has limitations, as it is not pressurized and therefore does not generate methane concentrations found in situ. The mere interest for using it was to study the response of AOM and the SMTZ to different fluid flow rates, which should always be kept in mind when interpreting the results. Please refer to Steeb et al. 2014 for more details on the method's advantages and disadvantages.

For SLOT experiments, two replicate multicorer cores from station SO206-31 (MUC) were sub-sampled with specific SLOT liners (inner diameter 6 cm) (Steeb et al. 2014). Liners were closed with rubber stoppers, sealed with electrical tape, transported (4°C) to the home laboratory and stored at 0°C in the dark until the experiment started (ca. 170 days after the MUC sampling). At GEOMAR, filters (glass fiber, Whatman GF/F) were applied at the bottom of the sediment core and at the lower and upper cap, as previously described (Steeb et al. 2014).

The following experimentations were conducted at 10°C (the in situ temperature was 8°C). Two different seawater media were applied: one medium, resembling seawater, was amended to natural sulfate concentrations (28 mmol l^{-1}). The added sulfate penetrated the sediment by diffusion, except for when porewater subsamples were taken with rhizons (see below), which temporarily facilitated a faster intrusion of sulfate-rich water from the supernatant and probably caused a smoothening of porewater profiles (Steeb et al. 2014). The other medium, resembling sulfate-free seepage fluid, carried dissolved methane (965 ± 180 µmol l^{-1}) upwards into the bottom of the core by advection. Both media were based on the sulfate reducer medium developed by Widdel and Bak (2006). In the "seepage" medium, $MgSO_4$ was replaced by MgCl. Both media were kept anoxic, and contained resazurin as oxygen indicator (Visser et al. 1990), with a pH adjusted to 7.5 and a salinity of 35 PSU. Bromide served as an inert tracer for the upward migration and was present only in the methane-enriched seepage medium (800 µmol l^{-1}). Hence, the depth where bromide and sulfate concentrations overlapped was interpreted as the SMTZ. We therefore used the sulfate-bromide transition zone (SBTZ) as a proxy for the SMTZ and defined it as the zone with the steepest SO_4^{2-} and

209 Br^- gradients. Medium composition and the gas headspace composition of the reservoirs are
210 summarized in Table 3.
211 SLOT experiments were performed with two sediment cores under different flow regimes (Table 4).
212 One core was exposed to a relatively moderate advective fluid flow velocity (10.6 cm yr^{-1}), here
213 further referred as the low flow core (LFC), whereas the other core was exposed to a 10-fold higher
214 advective fluid flow velocity (106.3 cm yr^{-1}), further referred as the high flow core (HFC). The
215 moderate fluid flow velocities were on the same order as those determined by the numerical model
216 (see Results). The high flow velocities were more than twice of those previously reported for Quepos
217 Slide (40 cm yr^{-1}; Karaca et al. 2012) and were employed to observe the sediment response under
218 extreme fluid flow. Similar or even higher (up to 200 cm yr^{-1}) advective flow velocities have been
219 reported for seeps within the same region (Hensen et al. 2004; Linke et al. 2005; Karaca et al. 2010;
220 Krause et al. 2014). The applied fluid flow velocities were strong enough to observe considerable
221 changes within the time frame of one year yet weak enough to avoid sulfate penetration to less than
222 one cm.
223 In the initial preparation phase of the experiment (40 days), the outflow of the system was located at
224 the bottom of the core and only methane-free seawater medium was pumped from top to bottom at
225 a pump rate of 20 µl min^{-1}. This procedure was applied to establish a homogeneous sulfate
226 distribution and anoxic conditions throughout the entire sediment column without disturbing the
227 sediment fabric, although some sediment compaction might occur. In the subsequent first
228 experimental phase, the outflow was mounted at the top of the core and seawater medium was
229 delivered to the overlying seawater at a pump rate of 20 µl min^{-1}. From this point, sulfate was
230 transported into the sediment core solely via diffusion, except for rhizon sampling (see above). From
231 the bottom, the seepage medium was supplied at 0.5 µl min^{-1} (LFC) and 5 µl min^{-1} (HFC) with an
232 average inflow methane concentration of 965 ± 180 µmol l^{-1}. Based on the pump rate, methane
233 concentration, and surface area of the sediment, a methane flux of 0.28 and 2.81 mmol m^{-2} d^{-1} was
234 calculated for the LFC and HFC core, respectively. These methane concentrations were lower than

235 those potentially encountered under in situ conditions because the cores were not pressurized,
236 resulting in lower methane fluxes (after Tishchenko et al. 2005; Karaca et al. 2012). After 260 d the
237 first experimental phase ended and the pump rates were increased from low to high flow velocities
238 for the LFC, and vice versa for the HFC. This switch marked the beginning of the second and final
239 experimental phase to study the response of AOM to rapid changes in the flow regime. After 316 d,
240 the experiment was terminated and the cores were sliced and sub-sampled for further analyses (see
241 below).

242 Methane emission from the sediment was calculated by multiplying the out-flow methane
243 concentrations (CH_{4out}) with the dilution factor (DF; 41 and 5 for LFC and HFC, respectively) and the
244 fluid flow (v; 10.6 and 106.3 cm yr^{-1} for LFC and HFC, respectively) according to equation (1).

245
$$CH_{4_{efflux}}\ [mmol\,m^{-2}\,d^{-1}] = v\ [cm\,yr^{-1}] \cdot CH_{4_{out}}\ [mmol\,cm^{-3}] \cdot DF \cdot \frac{10\,000}{365.25} \qquad (1)$$

246 Areal AOM rates (AOM_{areal}) were calculated from the difference between in- (CH_{4in}) and outflow
247 (CH_{4out}) methane concentrations before (258 d) and after (316 d) fluid flow velocity change according
248 to equation (2),

249
$$AOM_{areal}\ [mmol\,m^{-2}\,d^{-1}] = \left(\frac{CH_{4_{in}}\ [mmol\,cm^{-3}] - CH_{4_{out}}\ [mmol\,cm^{-3}] \cdot DF}{HRT\ [d]} \right) \cdot \frac{10\,000}{SLOT_{base}\ [cm^2]} \qquad (2)$$

250 with $SLOT_{base}$ for the base area of the SLOT-cores and DF for the dilution factor in the overlying water,
251 resulting from the different pump rates for the “seepage” and “seawater” media and their mixing in
252 the overlying water. HRT stands for the hydrological residence time, the average time of the seepage
253 medium to flow from the core inflow, through the sediment column, to the core outflow and was
254 calculated by dividing the water volume above and below the sediment core plus the sediment
255 porewater volume by the flow rate.

2.6 Geochemical parameters during SLOT experimentation: During the SLOT experiments, geochemical parameters were measured in 1 cm depth intervals throughout the sediment core. In addition, concentrations in the in- and out-flowing fluids were monitored. Sulfide concentrations, pH, and redox potential were measured with microsensors (sulfide needle sensor, H_2S-N, tip diameter 0.8 mm, Unisense; pH, MI 411 B, Gauge 20, Microelectrodes Inc.; redox potential needle sensors, MI-800, Gauge 25, Microelectrodes Inc.). Porewater samples (1.5 – 2 ml) for the determination of sulfate, bromide, and total alkalinity were obtained from each depth in the sediment using pre-installed rhizones (CSS-F, length 5 cm, diameter 2.5 mm, pore size 0.2 µm, Rhizosphere®). The in- and outflow of both cores were sampled with glass syringes for the determination of sulfate, bromide, total alkalinity and methane concentration. All sampling and measurement proceedings for the experiment are described in detail by Steeb et al. (2014). Given a removal of 8.1% porewater during each rhizon sampling, which causes mixing with adjacent layers, and an analytical precision of <1% (ion chromatography) and 0.1% (total alkalinity titration), we estimated a total analytical error of ca. 9% for sulfate and bromide, and 8.2% for total alkalinity, respectively.

2.7 Experiment termination and final sampling:

At the end of the experiment, 1.5 ml porewater from each depth was sampled for determinations of sulfide (0.5 ml), sulfate and bromide (0.5 ml) as well as total alkalinity (0.5 ml), and analyzed after the same methods as the ex situ porewater (see section 2.1).

After the final porewater sampling, sediment sub-samples were taken from each SLOT core. Two sub-cores (polycarbonate, length 260 mm, inner diameter 26 mm) were collected from each SLOT core for radiotracer determinations of AOM and sulfate reduction, and treated according to the protocols mentioned above. For the determination of methane concentrations, each SLOT core was sampled in 1 cm intervals (2 cm^3 volume sub-samples) using cut-off syringes (3 ml, PE). The sediment samples were transferred into glass vials (13 ml) with 5 ml 2.5% w/v NaOH. Vials were closed with butyl rubber stoppers and shaken directly after sampling. Methane was analyzed by gas chromatography (Hewlett Packard Series II) with a packed column (Haye SepT, 6 ft, 3.1 mm inner diameter, 100/120

mesh, Resteck, carrier gas: He 20 ml min^{-1}, combustion gas: synthetic air 240 ml min^{-1}, H_2 20 ml min^{-1}).

The remaining sediment of each SLOT core was sampled in 2 cm depth intervals. For porosity measurements, approximately 2 cm^3 samples were obtained using cut-off syringes (3 ml, PE), transferred to pre-weighed vials, and weighed, before and after the sample was freeze-dried. Porosity was then calculated by the difference in weight (Dalsgaard et al. 2000). Sub-samples of the dried sediment were used to determine total carbon (TC), total nitrogen (TN), total sulfur (TS) and total organic carbon (TOC) of the solid phase. TC, TN, TS, and TOC were analyzed using a CARLO ERBA Elemental Analyzer NA 1500. For TOC determination, inorganic carbon was removed by adding hydrochloric acid. Total inorganic carbon (TIC) was calculated from the difference between TC and TOC. All solid phase analyses were carried out in duplicates.

Further details on the SLOT sampling procedure and analytical procedures are described in Steeb et al. (2014).

3. Results:

3.1 Ex situ profiles and numerical models

Both MUC cores (SO206-29 MUC and SO206-31 MUC) were sampled at ~ 400 m water depth from sediments covered with sulfur bacteria mats, which are indicative for high methane fluxes (Torres et al. 2002; Treude et al. 2003).

At station SO-206-29 (MUC), sulfate decreased from 28 mmol l^{-1} at the sediment surface to zero at the bottom of the core (26 cm below sea floor (cmbsf)) (Fig. 1, A). Conversely, methane concentrations were low (0.0 – 0.1 mmol l^{-1}) in the upper 15 cmbsf and increased below this zone to a maximum of 2.4 mmol l^{-1} at the bottom (Fig. 1, A). Accordingly, the SMTZ was located at approximately 17.5 cmbsf. Two maxima in sulfate reduction rates were identified in one of the replicate cores at the top (up to 1821 nmol cm^{-3} d^{-1}) and between 12.5 and 22.5 cmbsf (up to 879 nmol cm^{-3} d^{-1}) (Fig. 1, B). AOM coincided with the second sulfate reduction maximum and reached rates up to 569 nmol cm^{-3} d^{-1} (Fig. 1, C). Sulfide and total alkalinity (TA) increased from the top (0.0 mmol l^{-1} and 2.5 meq l^{-1}, respectively) to a maximum within the SMTZ (7.9 mmol l^{-1} and 23.4 meq l^{-1}, respectively, at 17.5 cm sediment depth), (Fig. 1, D). Areal turnover rates of methane and sulfate integrated over the entire sediment depth of 26 cm were similar for AOM (on average 12.87 ± 5.98 mmol m^{-2} d^{-1}) and sulfate reduction (on average 13.38 ± SD 13.61 mmol m^{-2} d^{-1}) with a ratio of 0.96 (AOM : sulfate reduction), respectively.

The steady state model resulted in a fluid flow of 7 cm yr^{-1} and an areal AOM rate of 11.35 mmol m^{-2} d^{-1} (Table 2). In total, around 92% of the delivered methane was oxidized by AOM and ~8% was released to the seawater. Fitted porewater profiles and AOM rates are shown in Fig. 1.

In the second core, SO206-31 (MUC), sulfate decreased to 0 mmol l^{-1} within the first 15 cm sediment depth and considerable methane concentrations (> 3.4 mmol l^{-1}) were observed at 5 cmbsf (Fig. 2, A). The observed maximum methane concentration was 10.2 mmol l^{-1} (20.5 cmbsf). Accordingly, the SMTZ was located at approximately 5 - 15 cmbsf. Sulfate reduction and AOM occurred between 0 and 12.5 cmbsf with a sulfate reduction maximum (12052 nmol cm^{-3} d^{-1}) at the top of the SMTZ (~2.5

cmbsf) and an AOM maximum (1400 nmol cm^{-3} d^{-1}) in the upper part of the SMTZ (5.5 cm cmbsf) (Fig. 2, B, C). Highest sulfide and TA concentrations were measured within the SMTZ between 10 and 15 cmbsf (8.6 mmol l^{-1} and 24.1 meq l^{-1}, respectively) (Fig. 2, D). Areal sulfate reduction rates integrated over the entire sediment depth of 25 cm (218.90 ± 159.80 mmol m^{-2} d^{-1}) were around 5 times (AOM : SR = 0.21) higher compared to the areal rates of AOM (45.15 ± 11.48 mmol m^{-2} d^{-1}) integrated over of the same depth.

Replicate cores from SO206-31 taken for porewater and rate analyses showed a different depth of the SMTZ and the AOM peak, respectively. Based on this lateral heterogeneity, two different fits of AOM were applied in the numerical model: one for the porewater core (pw-fit) and one for the rate core (hf-fit), which required a higher fluid advection to align the modeled and measured AOM (details see Table 2). The pw-fit with 7 cm yr^{-1} fluid flow showed an efficient benthic filter which oxidized all delivered methane (9.09 mmol m^{-2} d^{-1}). The hf-fit (29 cm yr^{-1}) had an AOM rate of 41.69 mmol m^{-2} d^{-1} and oxidized around 93% of the delivered methane (45.09 mmol m^{-2} d^{-1}). Model results are shown in Fig. 2 and summarized in Table 2.

3.2 SLOT incubation experiments

For the SLOT-Incubations, two replicate cores from SO206-31 (MUC) were used.

3.2.1 Evolution of biogeochemical parameters during the main phase of the experiment (0-260 days):

The low fluid flow regime core

In the low flow regime core (LFC) incubations, **bromide** concentration, which was used as a tracer to track the seepage medium, was always very low and near detection limit (20 µmol l^{-1}). Values increased only weakly in the lowest 5 cm of the core, reaching a maximum of 45 µmol l^{-1} after 49 d (Fig. 3 D). After 105 d, a small concentration of bromide (< 3 mmol L^{-1}) appeared in the supernatant, which later (171 d) disappeared again. **Sulfate**, which was delivered from the top by diffusion,

348 decreased only slightly at the bottom of the core (27.2 mmol l^{-1}) due to a slow advection of methane-
349 enriched seepage medium. This was in accordance with the small increase in bromide (up to ~45
350 µmol l^{-1}). After 105 d, sulfate levels stabilized around 26 mmol l^{-1} at the bottom of the core and did
351 not further decrease during the low flow phase.
352 In the first 105 d, **sulfide** concentrations of the LFC core varied between 23 and 300 µmol l^{-1} over
353 depth with a maximum between 9 - 11 cm (Fig. 3 B, E, H). After 171 d, a sulfide peak (920 µmol l^{-1},
354 Fig. 3 K) occurred at 0.26 cm sediment depth, while no sulfide was detected in the overlying water.
355 Below the peak, sulfide varied between 300 and 500 µmol l^{-1}. Thirty days later (201 d runtime),
356 maximum sulfide concentrations of up to 230 µmol l^{-1} were observed between 1.5 and 10.7 cm
357 sediment depth (Fig. 3 N). After 258 d, directly before changing from low to high fluid flow, maximum
358 sulfide concentrations were 115 µmol l^{-1} at 4.5-5.5 cmbsf (Fig. 3, Q) and decreased to a minimum of
359 36 µmol l^{-1} near the sediment-water interface.
360 **Total Alkalinity (TA)** was predominantly lower inside the cores than in the media (30 meq l^{-1}). During
361 the LFC incubation, TA continuously decreased over the time from ~30 to ~24 meq l^{-1} below ~9 cm
362 (Fig. 3, B, E, H, K). After 171 d, TA varied between 28.7 and 21.7 meq l^{-1}. Directly before the change of
363 fluid flow (258 d), TA increased from the top (23.3 meq l^{-1}) to the bottom (26.7 meq l^{-1}; Fig. 3, Q).
364 Initial **redox potential** of the LFC was -50 mV at the top and around -150 mV below 2 cm sediment
365 depth (Fig. 3 C). After 49 d, the redox potential was more negative (-130 mV at top and between -160
366 to -270 mV below, Fig. 3, F); after 105 d, the redox potential increased to -80 mV at the top (Fig. 3, I).
367 Between 171 and 202 d runtime, the overlying water of the core showed a pink color caused by the
368 oxygen indicator resazurin. At the same time, the redox potential was positive (between 150 and 100
369 mV) at the sediment water interface (Fig. 3 L, O), probably as a result of oxygen intrusion.
370 Nevertheless, free oxygen should result in a redox potential >350 mV (Schulz 2000). We therefore
371 assume that oxygen was only temporally available and rapidly consumed. Deeper inside the
372 sediment, redox potential reached values between -200 and -400 mV (Fig. 3 L, O).

373 Directly before changing the fluid flow (258 d), the redox potential of the LFC was -100 mV in the
374 overlying water and around -200 mV inside the sediment (Fig. 3 R).
375 After 171 d runtime, **pH** was highest at the sediment-water interface (8.2, Fig. 3 L) and around 7.6
376 deeper in the sediment. Final pH before fluid flow swapping (258 d) decreased from 7.6 at the top to
377 7.1 at the bottom of the core (Fig. 3 R).
378 **Methane** concentrations in the out-flow of the LFC started at 1.5 µmol l^{-1} (29 d) and increased to 2.5
379 µmol l^{-1} after 105 d before decreasing again to 0.9 µmol l^{-1} after 258 d (Fig. 5). Calculated methane
380 efflux followed the methane concentration trend. The LFC methane efflux was between 0.011 and
381 0.030 mmol m^{-2} d^{-1}. AOM rates from the difference of in- and out-flow were 0.304 mmol m^{-2} d^{-1},
382 directly before changing the fluid flow regime. However, this rate must overestimate the actual AOM
383 activity, because the core did not reach steady state before the fluid flow change, as the bromide
384 front did not reach the sediment-water interface (see discussion).
385
386 *The high fluid flow regime core:*
387 In the high flow regime core (HFC), **bromide** quickly appeared after 21 d (400 µmol l^{-1}) at the bottom
388 of the core (Fig. 4, A). Bromide concentration continuously increased from the bottom towards the
389 top of the core until a chemocline developed between 4 and 10 cm sediment depth after 105 d (Fig.
390 4, G). This chemocline persisted during the remaining experiment and moved slowly upwards
391 reaching a zone between 1 and 6 cm depth after 258 d (Fig. 4, A, D). **Sulfate** concentrations during
392 the HFC period were opposite to the bromide distribution and coincided with the chemocline. Sulfate
393 continuously decreased towards the bottom of the core reaching the minimum concentration
394 (0.2 mmol l^{-1}) after 201 d (Fig. 4, M). Simultaneously, sulfate was more and more displaced from the
395 bottom to the top of the core, decreasing from 28.5 mmol l^{-1} to 12 mmol l^{-1} at the sediment-water
396 interface.
397 **Sulfide** concentrations were considerably lower compared to the LFC. At the beginning (21 d), sulfide
398 increased from the top (27 µmol l^{-1}) to 6 cm sediment depth (70 µmol l^{-1}) within the developing SBTZ

399 (Fig. 4, B), which was used as proxy for the SMTZ, and was constant at this level below 6 cm sediment
400 depth. In the following months, sulfide decreased below 20 µmol l^{-1} (105 d) and increased rapidly
401 after 171 d runtime at the top of the core to more than 500 µmol l^{-1} (Fig. 4, K). In the following
402 months, sulfide concentrations decreased again at first to maximum values of 300 µmol l^{-1} (4 cm
403 sediment depth, 202 d runtime) and to less than 60 µmol l^{-1} after 258 d (Fig. 4, Q).
404 **TA** in the HFC core showed similar trends as the LFC core. Near the start (21 d), TA decreased from 29
405 to 30 meq l^{-1} at the top of the core to 26 – 27 meq l^{-1} at the bottom (Fig. 4, B, E, H). After 171 d, this
406 distribution reversed with TA increasing from the top of the core to the bottom, from 21 - 26 meq l^{-1}
407 to 24 – 27 meq l^{-1} (Fig. 4, K).
408 The **redox potential** of the HFC core was, similar to the LFC core, highest at the sediment-water
409 interface and in the overlying water and lowest at larger depths of the core. Initially (21 d), redox
410 potential was -85 mV at the sediment water interface and between -100 and -150 mV in the
411 sediment (Fig. 4, C). Over time, the redox potential in the sediment became more negative, reaching
412 a value down to -385 mV after 105 d (Fig. 4 I, L). Between 105 to 202 d runtime, the overlying water
413 turned pink and showed a redox potential ranging from 100 to 200 mV (Fig. 4, Q), indicating oxygen
414 contamination in the core. Directly before the change in fluid flow, the redox potential returned to
415 negative values with -120 mV in the overlying water and around -200 mV in remaining core (Fig. 4, R).
416 Similar to the LFC core, the **pH** was highest at the sediment-water interface and lower inside the
417 sediment (8.1 – 7.8 after 171 d and 8.0 – 7.4 after 202 d; Fig. 4, L and O). Directly before the fluid
418 flow change (258 d), pH decreased to 7.6 at the sediment water interface and to 7.1-7.3 inside the
419 sediment (Fig. 4, R).
420 **Methane** concentration in the HFC outflow was initially (21 d) 7.5 µmol l^{-1} and then decreased to
421 1.7 µmol l^{-1} during the following 200 d. After 258 d runtime, methane concentration in the outflow
422 increased again to 2.8 µmol l^{-1}. Efflux of the HFC ranged from 0.025 up to 0.109 mmol m^{-2} d^{-1}.
423 Corresponding calculated AOM rates were 3.114 mmol m^{-2} d^{-1} directly before changing the flow rate
424 (258 d).

425 **3.2.2 Biogeochemical responses after changing the fluid flow regime (260-350 d runtime):**

426 After 260 d, the fluid flow in the cores was swapped from low to high and vice versa.

427 *New high flow regime core*

428 In the new high flow regime core (NHFC*, former LFC)* sulfate and bromide concentrations did not

429 change considerably over the entire runtime (350 d). TA remained constant at 25 meq l^{-1} (Fig. 3 T).

430 Sulfide concentrations were highest at 0.3 cm sediment depth (1230 µmol l^{-1}) and first decreased

431 steeply followed by a more steady increase (below 3 cm) with the exception of a second maximum

432 (625 µmol l^{-1}) at 5 cm. At the bottom of the core, a sulfide concentration of max 75 µmol l^{-1} was

433 reached. Redox potential was positive (31 mV) in the overlying water and between -280 and -330 mV

434 within the sediment (Fig. 3 U). The pH decreased from 8.5 to 7.5 between the sediment-water

435 interface and the bottom of the core.

436 Methane concentration of the outflow increased considerably from 0.9 to 11.6 µmol l^{-1} after 316 d

437 run time (Fig. 5). Calculated methane effluxes were 0.165 mmol m^{-2} d^{-1} and corresponding AOM rates

438 were 2.970 mmol m^{-2} d^{-1}. Similar to the LFC, the AOM rate is most likely overestimated, as the core

439 did not reach steady state (see discussion).

440 *New low flow regime core*

441 In the new low flow regime core (NLFC; *former HFC*), sulfate penetrated deeper and bromide

442 ascended less into the sediment, as compared to the profile prior to fluid flow change (Fig. 4, S).

443 Sulfide concentrations remained low, between 50 and 80 µmol l^{-1}, and TA varied between 23 and 25

444 meq l^{-1} (Fig. 4, T). Redox potential was positive (150 mV) at the sediment water interface and the

445 upper sediment (Fig. 4, U). Below 2 cm sediment depth, redox decreased to values between -200 and

446 -400 mV. The pH profile decreased from 8.05 in the overlying water and at the sediment-water

447 interface down to 7.55 below 6 cm sediment depth.

448 Methane concentrations in the outflow declined from 2.8 to 0.7 µmol l^{-1} (Fig. 5). Calculated methane

449 effluxes were 0.009 mmol m^{-2} d^{-1} with a corresponding AOM rate of 0.306 mmol m^{-2} d^{-1}.

450

3.2.3 Biogeochemical parameters after experiment termination:

After 350 d runtime, the experiment was terminated, porewater was sampled, and the sediment sub-sampled for further analyses. In both cores, methane concentrations determined after experiment termination (around 2.5 µmol l^{-1}) were only a minor fraction of the original inflow concentration (965 µmol l^{-1}), which was probably mostly attributed to methane losses during porewater extraction using rhizones directly before sediment sampling (Steeb et al. 2014). In the NHFC (= former LFC) methane concentrations varied between 2 and 4 µmol l^{-1} with a slight increase towards the bottom of the core (Fig. 6, A). Sulfate concentrations decreased slightly from 29.5 mmol l^{-1} at the top to 26.2 mmol l^{-1} at the bottom of the core (Fig. 6, B). Sulfide increased from 50 mmol l^{-1} at the sediment surface (0.3 cm) to a maximum of 125 µmol l^{-1} at 6 cm and decreased to 80 µmol l^{-1} at the bottom of the core (Fig. 6, C). AOM rates of the NHFC determined by radiotracer techniques showed highest values between 4 to 10 cm sediment depth (0.50 – 0.91 nmol cm^{-3} d^{-1}) and, in addition, increased from top (0.10 nmol cm^{-3} d^{-1}) to bottom (0.33 nmol cm^{-3} d^{-1}). Areal turnover rates of methane and sulfate integrated over the entire sediment core (0-15 cm) were 0.043 and 2.31 mmol m^{-2} d^{-1} for AOM and sulfate reduction, respectively.

In the NLFC (= former HFC), methane concentrations remained consistently low at around 2-4 µmol l^{-1} (Fig. 7, A). Sulfate was between 27 and 28.5 mmol l^{-1} within the upper first 6 cm and then decreased to 10 mmol l^{-1} below this depth (Fig. 7, B). Consistent with the steepest decrease in sulfate, sulfide increased to a maximum of 42 µmol l^{-1}. Highest AOM rates determined with radiotracer techniques were detected between 5 and 11 cm (0.4 - 1 nmol cm^{-3} d^{-1}, Fig. 7, A). Sulfate reduction rates ranged from 16.95 to 27.71 nmol cm^{-3} d^{-1} in the upper sediment (0 - 6 cm depth) and decreased to 7.96 nmol cm^{-3} d^{-1} at the bottom, which corresponded to a simultaneous decrease in sulfate at the bottom of the core (Fig. 6, A). Areal rates integrated over the entire sediment depth (14 cm) were 0.042 and 2.494 mmol m^{-2} d^{-1} for AOM and sulfate reduction, respectively.

The TC contents were similar in both, the NHFC and NLFC core, and varied between 4.97 and 6.05 dry wt.% (Fig. 8, A, Fig. 9 A). A carbon peak (6.05 dry wt.%, 7 cm sediment depth) resulted from higher

TIC (3.09 -3.16 dry wt.%) in both cores. TOC (2.90 – 3.62 dry wt.%) of the NHFC and NLFC did not differ considerable from ex situ data (2.91–3.40 dry wt.%). Atomic C/N ratios were higher in both flow-through cores (8.67 – 9.43) compared to ex situ values (7.61 – 8.88), while TS was slightly lower (0.82 – 1.18 compared to 0.94 - 1.27 dry wt.%), especially in the upper region (0 - 2 cm) of the NHFC (0.84 compared to 1.11 dry wt.%) and showed, in contrast to the ex-situ cores, no minimum at 4.5 cm sediment depth (Fig. 8, C; Fig. 9, C).

4. Discussion:

4.1 The impact of fluid seepage and related processes on porewater gradients:

Quepos Slide sediment cores that were studied ex situ showed a SMTZ and AOM peaks within the upper 20 cm of the sediment (Fig. 2). We are therefore confident that the SLOT experiments (core length 14-16 cm) contained the most active zone of the benthic methane filter. During the experiments, the depth of the SBTZ, as proxy for the SMTZ, was controlled by fluid flow and migrated over time. Fluid flow velocity in the low flow regime core (LFC, 10.6 cm yr^{-1}) was in the same range of fluid flow modeled from the ex situ data (5-29 cm yr^{-1}). In the high flow regime core (HFC, 106 cm yr^{-1}), the fluid flow was two to ten times higher compared to our modeled data and also higher than other values published for Quepos Slide (1-40 cm yr^{-1}, Karaca et al. 2012, Table 5); however, the flow was still in the range of neighboring seeps (0.1 – 200 cm yr^{-1}, Hensen et al. 2004; Linke et al. 2005; Karaca et al. 2010; Krause et al. 2013). During the entire LFC/NHFC experiment no SBTZ developed, and consequently no steady state was reached. The missing evolution of a SBTZ was probably the result of a high hydrological residence time of the seepage medium (696 d for the LFC and 69 d for the NHFC), which in this case means the average time for the fluid to pass the water volume below the core and the entire sediment core. Nevertheless, small amounts of the seepage fluid obviously passed through the entire sediment, probably facilitated through channeling (Torres et al. 2002; Wankel et al. 2012), as demonstrated by the presence of methane in the outflow (Fig. 5) and bromide in the supernatant (Fig. 3G). The fraction of seepage medium (calculated from Br^- concentration) emitted, relative to the total inflow seepage volume of the LFC, increased from 0% to 2.5% in the last phase (260 d) and further increased to 4% after the system was changed to high flow (NHFC). Low AOM activity was detected over the entire core after experiment termination with highest turnover between 7 and 9 cm sediment depth, while methane concentrations stayed continuously low around 2-3 µmol l^{-1} over the entire core (see sampling artifacts, section 3.2.3.). In the HFC experiment, the SBTZ and related AOM activity was much more pronounced than in the LFC. The SBTZ moved upwards from 14 cm (max. depth) to <6 cm, and dropped down to 10 cm sediment

depth during the subsequent low flow phase (NLFC). During the first phase, fluids and SBTZ showed continuous migration, which was fast initially and became slower towards the end. The relatively stable depth of the SBTZ at the end of the first experiment phase (0 - 260 d) indicated the transition to a quasi-steady state situation. Highest AOM rates, determined by radiotracer measurements after experiment termination, were found within this SBTZ (6 - 10 cm sediment depth).

Sulfide concentrations of the HFC were generally highest within the SBTZ. In the LFC experiment, sulfide peaks were relatively broad and not so distinct, which was probably the result of a broad dispersive mixing layer between seepage and seawater medium. Due to the low fluid flow, higher sulfide concentrations evolved in the LFC as compared to the HFC, where sulfide was probably flushed-out before it accumulated. Relatively low sulfide concentrations were also observed at Mound 11, a seep site with high AOM and sulfate reduction activity and high fluid flow (Hensen et al. 2004; Krause et al. 2014). In the LFC experiments, sulfide concentrations fluctuated over time. While the increase in sulfide concentration was most likely correlated with enhanced sulfate reduction, a decrease could be caused either by the precipitation of metal sulfides and/or by microbial oxidation of sulfide (chemosynthesis). Precipitation of metal sulfides is correlated with a drop in pH (Glud et al. 2007; Preisler et al. 2007), as it was observed in our study. Oxygen and nitrate are important electron acceptors for microbial oxidation of sulfide in seep habitats. However, free oxygen was probably available only temporally (if at all) in the overlying water of the core due to a sampling artifact (see results), which was in accordance with a redox potential of less than 300 mV (Schulz 2000). Moreover, sulfide oxidation with oxygen would create a drop in pH. Conversely, pH increased in the surface sediment, which could be caused by sulfide oxidation via dissimilatory nitrate reduction to ammonium. The process has been previously observed at the sediment-water interface of seeps system (de Beer et al. 2006). Nitrate availability in the seawater medium was limited (~4 $\mu mol\ l^{-1}$). Nevertheless, sulfide-oxidizing bacteria, such as *Beggiatoa* or *Thioploca* can accumulate nitrate in their vacuoles (Fossing et al. 1995; Preisler et al. 2007). Furthermore, sediment cores recovered from the field were covered by sulfide-oxidizing bacterial mats. Since oxygen concentration in the bottom

water was extremely low in this OMZ (< 22 µmol l^{-1}, Wyrtki 1962; Levin 2003), nitrate appears to be the most attractive electron acceptor for these sulfide oxidizers.

In summary, the observed increase in sulfide concentrations was most likely attributed to sulfate reduction activity, according to the development of the SBTZ. A loss of sulfide was caused by porewater flushing through advection, which was most pronounced in the HFC. Sulfide loss via oxidation with nitrate (top of the sediment) and sulfide precipitation (below 2 cm sediment depth) occured more likely in the LFC.

4.2 Microbial turnover rates and efficiency of the benthic methane filter

Table 5 provides an overview of parameters (fluid flow, methane emission, methane flux, AOM rate) from different methane seep locations. Integrated areal AOM rates (45.15 ± 11.48 mmol m^{-2} d^{-1}) of ex situ radiotracer measurements from the present study were in the upper range of previous modeled data (1.5 – 42.1 mmol m^{-2} d^{-1} Karaca et al. 2012) and moderate to high compared to other seep systems (Treude et al. 2003; Joye et al. 2004; Niemann et al. 2006; Knittel and Boetius 2009; Krause et al. 2014). In the SLOT experiments, the calculated methane flux (0.3 – 2.8 mmol m^{-2} d^{-1}) was lower compared to modeled flux (9.1 – 41.7 mmol m^{-2} d^{-1}) of the replicate core and at the lower limit of the previously modeled data (0.2 – 56.1 mmol m^{-2} d^{-1}, Karaca et al. 2012). However, fluxes of the SLOT experiment were still in the range of data published for seeps in this region (Mau et al. 2006; Karaca et al. 2010). In agreement with the relatively low methane flux during the SLOT experiment, AOM rates (determined from the difference in methane concentration between in and outflow) were 1 to 2 orders of magnitude lower compared to ex situ determinations. AOM rates determined with radiotracer measurements after experiment termination revealed peaks within the SBTZ (proxy for the SMTZ) of the HFC (4 - 10 cmbsf). A broader distribution of AOM was found in the LFC, while similar integrated rates suggest the same potential for AOM. This agreement of integrated AOM rates despite differences in fluid flux illustrates a widening of the AOM zone with lower fluid fluxes, while a narrow AOM zone at high fluxes appears to be compensated by higher methane turnover. This effect was also reflected in a more distinct peak of sulfide (see above) and confirmed

by simulations in the numerical model, specifically at the two model runs from SO206-31 (MUC) (Fig. 1 and 2). However, it should be kept in mind that methane concentrations during the experiment were much lower than under in situ pressure and it is therefore difficult to predict the upper limit of the balance between fluid flux and AOM activity.

While in a previous study the methane consumption efficiency of the benthic filter was estimated to range between 23 and 96% of the methane flux (Karaca et al. 2012), the efficiency in our study was between 92 and 100% in the modeled ex situ data and 99% for the SLOT setup. The latter value is based on the assumption that steady-state conditions were reached in the SLOT cores directly before fluid flow change, which was most likely reached in the HFC, but not in the LFC (see discussion above). A reason for the partial disagreement in efficiency of the benthic filter compared to the earlier studies could be the natural variability of methane fluxes in this highly heterogeneous area. While Karaca et al. (2012) based their results on a large number of sediment cores (20 cores from the same seep site), only two randomly chosen sites were sampled in our study, and only one was used for the experiment. Another explanation could be temporal variability of fluid and methane flux. Karaca et al. (2012) conducted their study 10 years prior to ours. Methane flux as well as microbial activity could have changed easily over this period (Mau et al. 2007; Füri et al. 2010). A drop in methane flux would probably enhance the efficiency of the benthic methane filter. For example, in the present experiment, methane fluxes were 2 to 33 times lower compared to the model of Karaca et al. (2012) since the system was not pressurized and hence the solubility of methane was limited. Lower methane fluxes resulted in a high efficiency of the benthic microbial methane filter, despite relatively high fluid advection.

Radiotracer determination of microbial turnover rates after the experiment revealed sulfate reduction activity at levels higher than AOM, which was probably partly coupled to organic matter degradation. Since the cores were obtained within an oxygen minimum zone, sulfate reduction is supposedly the most important pathway for organic matter degradation (Jørgensen 1977; Sørensen et al. 1979; Bohlen et al. 2011). High C/N ratios in cores of the terminated experiment compared to

ex situ cores (Fig. 8 and 9) support this assumption, because advanced microbial degradation of fresh organic matter with high nitrogen content leads to a shift from low to high C/N ratios (Whiticar 2002). We assume that at most 80% of the sulfate reduction in the ex situ analyses of SO206-St31 (MUC) can be related to organic matter degradation (AOM : SR = 0.21). Most likely, this ratio was less, because ex situ radiotracer incubations were conducted under atmospheric pressure and less methane was available compared to the in situ conditions. However, because organoclastic sulfate reduction occurred ex situ at the sediment-water interface (0 - 2 cmbsf, Fig. 1 and 2), where the consumed sulfate is replenished relatively rapidly by diffusion and mixing from the seawater, this surface activity has probably only little effect on sulfate gradients deeper in the sediment (Jørgensen et al. 2001; Karaca et al. 2012).

In Summary, the benthic microbial methane filter at Quepos Slide was found to be very efficient under continuous flow. Only increases in fluid and methane flux, such as at the beginning of the experiment or more pronounced after the fluid flow change, led to a drop in efficiency. Once a new steady state situation establishes, higher fluxes are expected to be compensated by a more intensive AOM zone (see above).

4.3 Response time of the microbial benthic methane filter:

In the outflow of the LFC, methane concentrations increased only little and decreased after 202 d (directly before fluid flow change) to the initial concentration. In contrast, methane concentrations in the outflow of the HFC core were high (7.5 µmol l^{-1}) at the beginning (29 d) and decreased quasi-exponentially to concentrations of ~2 µmol l^{-1} after 171 d. In the same time interval, the fraction of the methane-containing “seepage” medium at the sediment-water interface, calculated from the tracer (bromide) concentrations, changed from 13% to 34%, (Fig. 4 A, J). From the delivered methane (125.5 and 376.4 µmol l^{-1}) 30% and 98%, was oxidized after 29 and 171 d, respectively, in the HFC. This period (0-171 d) can be interpreted as the response time of the benthic microbial methane filter in the sediments of Quepos Slide. After change of the flow regime, the efflux of methane suddenly reduced to only 22% (0.009 mmol m^{-2} d^{-1}) in the former HFC (=NLFC), while the efflux in the former

LFC (=NHFC) increased rapidly 15-fold (0.169mmol m^{-2} d^{-1}) after changing the fluid flow. Based on bromide concentrations, the fraction of seepage medium in the outflow of the NHFC was 4%, which should theoretically equal 38.5 µmol l^{-1} methane in the outflow, if no methane would be consumed. Compared to methane concentrations directly measured in the outflow, only ~70% of the inflow methane was oxidized and 30% was emitted.

These results illustrate how sudden events could result in an abrupt increase in methane efflux. Mau et al. (2006) attributed fluctuations of methane concentrations in the water column, which occurred between autumn 2002 and 2003 at the Costa Rican seeps, to an earthquake in June 2002. However, it was not specified if the increased methane flux resulted from increased fluid flow, or simply from bubble release or if it was a continuous increase of methane flux or just a transient effect.

The experiments of the present study clearly show that the benthic microbial methane filter is able to respond within a relatively brief time of 5-6 months to increased methane fluxes and leads to the development of a much shallower and thinner AOM zone. Even if methane fluxes and methane concentrations were four times higher in situ, as expected from modeled methane fluxes of this study, the benthic microbial methane filter may still be able to respond quickly if a methanotrophic community is already fully established. Outside of seep habitats, where the microbial benthic methane filter is either absent or in deeper sediment zones, the adaptation might require much more time, since the doubling rate of the microbes involved is in the order of a few months (Girguis et al. 2005; Nauhaus et al. 2007; Krüger et al. 2008; Meulepas et al. 2009). Mau et al. (2007) observed a reduction of methane emissions in the water column above the earthquake-impacted seepage area by 50-90% in a period of one year. In our experiments, the benthic microbial methane filter required only ~170 d to adapt to the new flow regime. It is not clear, if the subsequent reduction of methane emissions observed by Mau et al. (2007) was the result of an ephemeral pulse of methane flux or by the adaption of the microbial benthic methane filter. Our results indicate that at least both situations are conceivable.

638 Another scenario, in which the benthic methane filter would be challenged, is the destabilization of
639 gas hydrates as a result of climate change (Buffett and Archer 2004). However, due to retarded heat
640 flux into deeper sediment layers, dissociation of considerable gas hydrate volumes probably require
641 hundreds to thousands of years (Biastoch et al. 2011). In the present study, we demonstrate that an
642 established microbial benthic methane filter can compensate relatively abrupt increases in methane
643 flux. Only "pristine" sediments, which are virtually devoid of methanotrophs are expected to show
644 long adaptations periods of up to several years or even decades (Dale et al. 2008) due to slow growth
645 rates of the anaerobes (Girguis et al. 2005; Nauhaus et al. 2007; Goffredi et al. 2008).

5. Conclusions:

Surface sediments of the Quepos Slide, a cold seep on the Pacific coastline of Costa Rica located within the Eastern Tropical North Pacific oxygen minimum zone, feature a very efficient benthic methane filter, demonstrated by direct measurements of methane turnover rates ex situ and numerical reaction modeling. In vitro experiments with intact sediment cores using a sediment-flow-through system further allowed following the adaptation of the SMTZ to changes in fluid flow, which revealed that the SMTZ narrows to a thin layer under high fluid flow conditions. Methane (ca. 1 mmol L^{-1} at atmospheric pressure) transported under high fluid flow was efficiently consumed (99% oxidation) by the benthic methane filter after a response period of ca. 170 d. These results illustrate how an established benthic methanotrophic microbial community could react to pulses in fluid and methane flow induced, for example, by earthquakes or gas hydrate dissociation, and how it regains its efficiency level after passing through a non-steady state period. As we here present only one example of a response to a sudden fluid flow pulse, further studies from other seep systems are advisable to validate our results.

Author contribution:

TT, PL, and CH initiated this study. PS, SK, MN, AD, sampled the sediment. SK and PS performed the radiotracer incubations. On board, AD was responsible for porewater measurements and MN conducted the methane measurements. CH and PS carried out the numerical modeling with input from AD. SK and PS carried out rate measurements and turnover calculations. Experiments were designed by TT and PL. Experiments were performed by PS including measurements and calculations. PS wrote the manuscript with input TT, PL, and AD as well as other co-authors.

Acknowledgments:

We thank the captain and the crew of R/V *SONNE* and all staff members who this supported work onboard. Special thanks goes to B. Domeyer, A. Bleyer, R. Ebbinghaus, R. Surberg, E. Corrales-Cordero, and E. Pinero for technical support during porewater analyzes. K. Kretschmer is thanked for help during maintenance of the SLOT-system. K. Kretchmer, J. Farkas, and J. Hommer are thanked for technical support during radiotracer analyzes. We thank three anonymous referees and P. Dando for their helpful comments on the submitted manuscript. This project was financed through the Collaborative Research Center (SFB) 574 "Volatiles and Fluids in Subduction Zones" and the Cluster of Excellence "The Future Ocean" funded by the German Research Foundation (DFG). M. Nuzzo was funded by the Portuguese Science and Technology Foundation post-doctoral fellowship FCT-SFRH/BPD/44598/2008.

References:

Aiello, I. W. 2005. Fossil seep structures of the Monterey Bay region and tectonic/structural controls on fluid flow in an active transform margin. Palaeogeogr. Palaeoclimatol. Palaeoecol. **227**: 124–142.

De Beer, D., E. Sauter, H. Niemann, N. Kaul, U. Witte, M. Schlüter, and A. Boetius. 2006. In situ fluxes and zonation of microbial activity in surface sediments of the Håkon Mosby Mud Volcano. Limnol. Oceanogr. **51**: 1315–1331.

Biastoch, A., T. Treude, L. H. Rüpke, U. Riebesell, C. Roth, E. B. Burwicz, W. Park, M. Latif, C. W. Böning, G. Madec, and K. Wallmann. 2011. Rising Arctic Ocean temperatures cause gas hydrate destabilization and ocean acidification. Geophys. Res. Lett. **38**: 1–5.

Boetius, A., K. Ravenschlag, C. J. Schubert, D. Rickert, F. Widdel, A. Gieseke, R. Amann, B. B. Jørgensen, U. Witte, O. Pfannkuche, and B. B. Jorgensen. 2000. A marine microbial consortium apparently mediating anaerobic oxidation of methane. Nature **407**: 623–626.

Bohlen, L., A. W. Dale, S. Sommer, T. Mosch, C. Hensen, A. Noffke, F. Scholz, and K. Wallmann. 2011. Benthic nitrogen cycling traversing the Peruvian oxygen minimum zone. Geochim. Cosmochim. Acta **75**: 6094–6111.

Bohrmann, G., K. Heeschen, C. Jung, W. Weinrebe, B. Baranov, R. Heath, V. Hu, M. Hort, and D. Masson. 2002. Widespread fluid expulsion along the seafloor of the Costa Rica convergent margin. Terra Nov. **14**: 69–79.

Borowski, W. S., C. K. Paull, and W. Ussler III. 1996. Marine pore-water sulfate profiles indicate in situ methane flux from underlying gas hydrate. Geology **24**: 655–658.

Borowski, W. S., C. K. Paull, and W. Ussler III. 1999. Global and local variations of interstitial sulfate gradients in deep-water, continental margin sediments: Sensitivity to underlying methane and gas hydrates. Mar. Geol. **159**: 131–154.

Buffett, B., and D. Archer. 2004. Global inventory of methane clathrate: sensitivity to changes in the deep ocean. Earth Planet. Sci. Lett. **227**: 185–199.

Burwicz, E., L. Rüpke, and K. Wallmann. 2011. Estimation of the global amount of submarine gas hydrates formed via microbial methane formation based on numerical reaction-transport modeling and a novel parameterization of Holocene sedimentation. Geochim. Cosmochim. Acta **75**: 4562–4576.

Cline, J. 1969. Spectrophotometric determination of hydrogen sulfide in natural waters. Limnol. Oceanogr. **14**: 454–458.

Crutchley, G. J., D. Klaeschen, L. Planert, J. Bialas, C. Berndt, C. Papenberg, C. Hensen, M. J. Hornbach, S. Krastel, and W. Brueckmann. 2014. The impact of fluid advection on gas hydrate stability: Investigations at sites of methane seepage offshore Costa Rica. Earth Planet. Sci. Lett. **401**: 95–109.

718 Dale, A. W., V. Brüchert, M. Alperin, and P. Regnier. 2009. An integrated sulfur isotope model for
719 Namibian shelf sediments. Geochim. Cosmochim. Acta **73**: 1924–1944.

720 Dale, A. W., P. Van Cappellen, D. R. Aguilera, and P. Regnier. 2008. Methane efflux from marine
721 sediments in passive and active margins: Estimations from bioenergetic reaction–transport
722 simulations. Earth Planet. Sci. Lett. **265**: 329–344.

723 Dalsgaard, T., L. P. Nielsen, V. Brotas, P. Viaroli, G. Underwood, D. Nedwell, K. Sundbäck, S. Rysgaard,
724 A. Miles, M. Bartoli, L. Dong, D. C. O. Thornton, L. D. M. Ottosen, G. Castaldelli, and N. Risgaard-
725 Petersen. 2000. Sediment Characteristics, p. 53–54. *In* Protocol Handbook for NICE- Nitrogen
726 Cycling in Esturies: a project under EU research programme: Marine Science and Technology
727 (MAST III). National Environmental Research Institute.

728 Ettwig, K. F., M. K. Butler, D. Le Paslier, E. Pelletier, S. Mangenot, M. M. M. Kuypers, F. Schreiber, B. E.
729 Dutilh, J. Zedelius, D. de Beer, J. Gloerich, H. J. C. T. Wessels, T. van Alen, F. Luesken, M. L. Wu,
730 K. T. van de Pas-Schoonen, H. J. M. Op den Camp, E. M. Janssen-Megens, K.-J. Francoijs, H.
731 Stunnenberg, J. Weissenbach, M. S. M. Jetten, and M. Strous. 2010. Nitrite-driven anaerobic
732 methane oxidation by oxygenic bacteria. Nature **464**: 543–8.

733 Fischer, D., J. M. Mogollón, M. Strasser, T. Pape, G. Bohrmann, N. Fekete, V. Spiess, and S. Kasten.
734 2013. Subduction zone earthquake as potential trigger of submarine hydrocarbon seepage. Nat.
735 Geosci. **6**: 647–651.

736 Fischer, D., H. Sahling, and K. Nöthen. 2012. Interaction between hydrocarbon seepage,
737 chemosynthetic communities, and bottom water redox at cold seeps of the Makran
738 accretionary prism: insights from habitat-specific pore water sampling and modeling.
739 Biogeochemistry **9**: 2013–2031.

740 Fossing, H., V. Gallardo, B. Jørgensen, M. Hüttel, L. P. Nielson, H. Schulz, D. E. Canfield, S. Forster, R.
741 N. Glud, J. K. Gundersen, J. Küver, N. B. Ramsing, A. Teske, B. Thamdrup, and O. Ulloa. 1995.
742 Concentration and transport of nitrate by the mat-forming sulphur bacterium Thioploca. Nature
743 **374**: 714–715.

744 Füri, E., D. R. Hilton, M. D. Tryon, K. M. Brown, G. M. McMurtry, W. Brückmann, and C. G. Wheat.
745 2010. Carbon release from submarine seeps at the Costa Rica fore arc: Implications for the
746 volatile cycle at the Central America convergent margin. Geochemistry, Geophys. Geosystems
747 **11**, doi:10.1029/2009GC002810

748 Girguis, P., A. Cozen, and E. DeLong. 2005. Growth and population dynamics of anaerobic methane-
749 oxidizing archaea and sulfate-reducing bacteria in a continuous-flow bioreactor. Appl. Environ.
750 Microbiol. **71**: 3725–3733.

751 Glud, R. N., P. Berg, H. Fossing, and B. B. Jørgensen. 2007. Effect of the diffusive boundary layer on
752 benthic mineralization and O2 distribution: A theoretical model analysis. Limnol. Oceanogr. **52**:
753 547–557.

754 Goffredi, S. K., R. Wilpiszeski, R. Lee, and V. J. Orphan. 2008. Temporal evolution of methane cycling
755 and phylogenetic diversity of archaea in sediments from a deep-sea whale-fall in Monterey
756 Canyon, California. ISME J. **2**: 204–20.

757 Haese, R.R., C. Meile, P.V. Cappellen, G.J. De Lange. 2003. Carbon geochemistry of cold seeps:
758 methane fluxes and transformation in sediments from Kazan mud volcano, eastern
759 Mediterranean Sea, Earth Planet. Sci. Lett. **212**: 361–375.

760 Han, X., E. Suess, H. Sahling, and K. Wallmann. 2004. Fluid venting activity on the Costa Rica margin:
761 new results from authigenic carbonates. Int. J. Earth Sci. **93**: 596–611.

762 Harders, R., C. R. Ranero, W. Weinrebe, and J. H. Behrmann. 2011. Submarine slope failures along the
763 convergent continental margin of the Middle America Trench. Geochemistry Geophys.
764 Geosystems **12**, doi:10.1029/2010GC003401

765 Henrys, S., M. Reyners, I. Pecher, S. Bannister, Y. Nishimura, and G. Maslen. 2006. Kinking of the
766 subducting slab by escalator normal faulting beneath the North Island of New Zealand. Geology
767 **34**: 777.

768 Hensen, C., and K. Wallmann. 2005. Methane formation at Costa Rica continental margin—
769 constraints for gas hydrate inventories and cross-décollement fluid flow. Earth Planet. Sci. Lett.
770 **236**: 41–60.

771 Hensen, C., K. Wallmann, M. Schmidt, C. R. Ranero, and E. Suess. 2004. Fluid expulsion related to
772 mud extrusion off Costa Rica—A window to the subducting slab. Geology **32**: 201.

773 Hesse, R., S. K. Frape, P. K. Egeberg, and R. Matsumoto. 2000. Stable Isotope Studies (Cl, O, and H) of
774 Interstitial Waters from Site 997, Blake Ridge Gas Hydrate Field, West Atlantic. Proc. Ocean Drill.
775 Program, Sci. results **164**: 129–137.

776 Hinrichs, K., and A. Boetius. 2002. The anaerobic oxidation of methane: new insights in microbial
777 ecology and biogeochemistry, p. 457–477. *In* G. Wefer, D. Billet, D. Hebbeln, B. Jørgensen, M.
778 Schlüter, and T. Van Weering [eds.], Ocean Margin Systems. Springer-Verlag Berlin Heidelberg.

779 Ivanenkov, V. N., and Y. I. Lyakhin. 1978. Determination of total alkalinity in seawater, p. 110–114. *In*
780 O.K. Bordovsky and V.N. Ivanenkov [eds.], Methods of Hydrochemical Investigations in the
781 Ocean. Nauka Publ. House.

782 Jørgensen, B. B. 1977. The Sulfur Cycle of a Coastal Marine Sediment (Limfjorden, Denmark). Limnol.
783 Oceanogr. **22**: 814–832.

784 Jørgensen, B. B. 1978. A comparison of methods for the quantification of bacterial sulfate reduction
785 in coastal marine sediments. 1. Measurements with radiotracer techniques. Geomicrobiol. J **1**:
786 11–27.

787 Jørgensen, B., A. Weber, and J. Zopfi. 2001. Sulfate reduction and anaerobic methane oxidation in
788 Black Sea sediments. Deep Sea Res. Part I Oceanogr. Res. Pap. **48**: 2097–2120.

789 Joye, S. B., A. Boetius, B. N. Orcutt, J. P. Montoya, H. N. Schulz, M. J. Erickson, and S. K. Lugo. 2004.
790 The anaerobic oxidation of methane and sulfate reduction in sediments from Gulf of Mexico
791 cold seeps. Chem. Geol. **205**: 219–238.

792 Judd, A., M. Hovland, and L. Dimitrov. 2002. The geological methane budget at continental margins
793 and its influence on climate change. Geofluids **2**: 109–126.

794 Kallmeyer, J., T. G. Ferdelman, A. Weber, H. Fossing, and B. B. Jørgensen. 2004. A cold chromium
795 distillation procedure for radiolabeled sulfide applied to sulfate reduction measurements.
796 Limnol. Oceanogr. Methods **2**: 171–180.

797 Karaca, D., C. Hensen, and K. Wallmann. 2010. Controls on authigenic carbonate precipitation at cold
798 seeps along the convergent margin off Costa Rica. Geochemistry Geophys. Geosystems **11**: 1–
799 19.

800 Karaca, D., T. Schleicher, C. Hensen, P. Linke, and K. Wallmann. 2012. Quantification of methane
801 emission from bacterial mat sites at Quepos Slide offshore Costa Rica. Int. J. Earth Sci. 1–25.

802 Kluesner, J. W., E. A. Silver, N. L. Bangs, K. D. McIntosh, J. Gibson, D. Orange, C. R. Ranero, and R. von
803 Huene. 2013. High density of structurally controlled, shallow to deep water fluid seep indicators
804 imaged offshore Costa Rica. Geochemistry, Geophys. Geosystems **14**: 519–539.

805 Knittel, K., and A. Boetius. 2009. Anaerobic oxidation of methane: progress with an unknown process.
806 Annu. Rev. Microbiol. **63**: 311–34.

807 Krause, S., P. Steeb, C. Hensen, V. Liebetrau, A. W. Dale, M. Nuzzo, and T. Treude. 2014. Microbial
808 activity and carbonate isotope signatures as a tool for identification of spatial differences in
809 methane advection: a case study at the Pacific Costa Rican margin. Biogeosciences **11**: 507–523.

810 Krüger, M., M. Blumenberg, S. Kasten, A. Wieland, L. Känel, J. Klock, W. Michaelis, and R. Seifert.
811 2008. A novel, multi-layered methanotrophic microbial mat system growing on the sediment of
812 the Black Sea. Environ. Microbiol. **10**: 1934–47.

813 Kutterolf, S., V. Liebetrau, T. Mörz, A. Freundt, T. Hammerich, and D. Garbe-Schönberg. 2008.
814 Lifetime and cyclicity of fluid venting at forearc mound structures determined by
815 tephrostratigraphy and radiometric dating of authigenic carbonates. Geology **36**: 707.

816 Kvenvolden, K. 2002. Methane hydrate in the global organic carbon cycle. Terra Nov. **14**: 302–306.

817 Lein, A., P. Vogt, K. Crane, A. Egorov, M. Ivanov. 1999. Chemical and isotopic evidence for the nature
818 of the fluid in CH_4-containing sediments of the Hakon Mosby Mud Volcano, Geo. Mar. Lett. **19:**
819 76–83.

820 Levin, L. A. 2003. Oxygen Minimum Zone Benthos : Adaption and Community. Ocean. Mar. Biol. an
821 Annu. Rev. **41**: 1–45.

822 Linke, P., K. Wallmann, E. Suess, C. Hensen, and G. Rehder. 2005. In situ benthic fluxes from an
823 intermittently active mud volcano at the Costa Rica convergent margin. Earth Planet. Sci. Lett.
824 **235**: 79–95.

825 Mau, S., G. Rehder, I. G. Arroyo, J. Gossler, and E. Suess. 2007. Indications of a link between
826 seismotectonics and CH 4 release from seeps off Costa Rica. Geochemistry, Geophys.
827 Geosystems **8**: 1–13.

828 Mau, S., G. Rehder, H. Sahling, T. Schleicher, and P. Linke. 2012. Seepage of methane at Jaco Scar, a
829 slide caused by seamount subduction offshore Costa Rica. Int. J. Earth Sci. , doi:10.1007/s00531-
830 012-0822-z

Mau, S., H. Sahling, G. Rehder, E. Suess, P. Linke, and E. Soeding. 2006. Estimates of methane output from mud extrusions at the erosive convergent margin off Costa Rica. Mar. Geol. **225**: 129–144.

Meulepas, R. J. W., C. G. Jagersma, J. Gieteling, C. J. N. Buisman, A. J. M. Stams, and P. N. L. Lens. 2009. Enrichment of anaerobic methanotrophs in sulfate-reducing membrane bioreactors. Biotechnol. Bioeng. **104**: 458–70.

Milucka, J., T. G. Ferdelman, L. Polerecky, D. Franzke, G. Wegener, M. Schmid, I. Lieberwirth, M. Wagner, F. Widdel, and M. M. M. Kuypers. 2012. Zero-valent sulphur is a key intermediate in marine methane oxidation. Nature **2**: 1–23.

Minami, H., K. Tatsumi, A. Hachikubo, S. Yamashita, H. Sakagami, N. Takahashi, H. Shoji, Y. K. Jin, A. Obzhirov, N. Nikolaeva, and A. Derkachev. 2012. Possible variation in methane flux caused by gas hydrate formation on the northeastern continental slope off Sakhalin Island, Russia. Geo-Marine Lett. **32**: 525–534.

Nauhaus, K., M. Albrecht, M. Elvert, A. Boetius, and F. Widdel. 2007. In vitro cell growth of marine archaeal-bacterial consortia during anaerobic oxidation of methane with sulfate. Environ. Microbiol. **9**: 187–96.

Niemann, H., T. Lösekann, D. de Beer, M. Elvert, T. Nadalig, K. Knittel, R. Amann, E. J. Sauter, M. Schlüter, M. Klages, J. P. Foucher, and A. Boetius. 2006. Novel microbial communities of the Haakon Mosby mud volcano and their role as a methane sink. Nature **443**: 854–8.

Orcutt, B. N., J. B. Sylvan, N. J. Knab, and K. J. Edwards. 2011. Microbial ecology of the dark ocean above, at, and below the seafloor. Microbiol. Mol. Biol. Rev. **75**: 361–422.

Pimenov, N., A. Savvichev, I. Rusanov, A. Lein, A. Egorov, A. Gebruk, L. Moskalev, P. Vogt. 1999. Microbial processes of carbon cycle as the base of food chain of Hakon Mosby Mud Volcano benthic community, Geo Mar. Lett. **19:** 89–96.

Preisler, A., D. de Beer, A. Lichtschlag, G. Lavik, A. Boetius, and B. B. Jørgensen. 2007. Biological and chemical sulfide oxidation in a Beggiatoa inhabited marine sediment. ISME J. **1**: 341–53.

Ranero, C., and R. von Huene. 2000. Subduction erosion along the Middle America convergent margin. Nature **404**: 748–52.

Ranero, C. R., I. Grevemeyer, H. Sahling, U. Barckhausen, C. Hensen, K. Wallmann, W. Weinrebe, P. Vannucchi, R. von Huene, and K. McIntosh. 2008. Hydrogeological system of erosional convergent margins and its influence on tectonics and interplate seismogenesis. Geochemistry Geophys. Geosystems **9**, doi:10.1029/2007GC001679

Reeburgh, W. S. 2007. Oceanic methane biogeochemistry. Chem. Rev. **107**: 486–513.

Sahling, H., D. G. Masson, C. R. Ranero, V. Hühnerbach, W. Weinrebe, I. Klaucke, D. Bürk, W. Brückmann, and E. Suess. 2008. Fluid seepage at the continental margin offshore Costa Rica and southern Nicaragua. Geochemistry, Geophys. Geosystems **9**: 1–22.

Sahling, H., D. Rickert, R. W. Lee, P. Linke, and E. Suess. 2002. Macrofaunal community structure and sulfide flux at gas hydrate deposits from the Cascadia convergent margin, NE Pacific. Mar. Ecol. Prog. Ser. **231**: 121–138.

Schmidt, M., C. Hensen, T. Mörz, C. Müller, I. Grevemeyer, K. Wallmann, S. Mau, and N. Kaul. 2005. Methane hydrate accumulation in “Mound 11” mud volcano, Costa Rica forearc. Mar. Geol. **216**: 83–100.

Schulz, H. D. 2000. Redox Measurements in Marine Sediments, p. 235–246. *In* J. Schüring, H.D. Schulz, J. Böttcher, and W.H.M. Duijnisveld [eds.], REDOX: Fundamentals, Processes, and Applications. Springer Berlin.

Sørensen, J., B. Jørgensen, and N. Revsbech. 1979. A comparison of oxygen, nitrate, and sulfate respiration in coastal marine sediments. Microb. Ecol. **5**: 105–115.

Sommer, S., O. Pfannkuche, P. Linke, R. Luff, J. Greinert, M. Drews, S. Gubsch, M. Pieper, M. Poser, T. Viergutz. 2006. Efficiency of the benthic filter: Biological control of the emission of dissolved methane from sediments hosting shallow gas hydrates at Hydrate Ridge. Global Biogeochem. Cycles **20:** GB2019, doi:10.1029/2004GB002389

Steeb, P., P. Linke, and T. Treude. 2014. A sediment flow-through system to study the impact of shifting fluid and methane flow regimes on the efficiency of the benthic methane filter. Limnol. Oceanogr. Methods **12**: 25–45.

Suess, E. 2010. Marine Cold Seeps, p. 188–198. *In* K.N. Timmis [ed.], Handbook of Hydrocarbon and Lipid Microbiology. Springer Berlin Heidelberg.

Syracuse, E. M., and G. a. Abers. 2006. Global compilation of variations in slab depth beneath arc volcanoes and implications. Geochemistry, Geophys. Geosystems **7**: 1–18.

Tishchenko, P., C. Hensen, K. Wallmann, and C. S. Wong. 2005. Calculation of the stability and solubility of methane hydrate in seawater. Chem. Geol. **219**: 37–52.

Torres, M. E. E., K. Wallmann, A. M. M. Tréhu, G. Bohrmann, W. S. Borowski, and H. Tomaru. 2004. Gas hydrate growth, methane transport, and chloride enrichment at the southern summit of Hydrate Ridge, Cascadia margin off Oregon. Earth Planet. Sci. Lett. **226**: 168–175.

Torres, M. E., J. McManus, D. E. Hammond, M. A. de Angelis, K. U. Heeschen, S. L. Colbert, M. D. Tryon, K. M. Brown, and E. Suess. 2002. Fluid and chemical fluxes in and out of sediments hosting methane hydrate deposits on Hydrate Ridge, OR, I: Hydrological provinces. Earth Planet. Sci. Lett. **201**: 525–540.

Treude, T., A. Boetius, K. Knittel, K. Wallmann, and B. Barker Jørgensen. 2003. Anaerobic oxidation of methane above gas hydrates at Hydrate Ridge, NE Pacific Ocean. Mar. Ecol. Prog. Ser. **264**: 1–14.

Treude, T., M. Krüger, A. Boetius, and B. Jørgensen. 2005. Environmental control on anaerobic oxidation of methane in the gassy sediments of Eckernfoerde Bay(German Baltic). Limnol. Oceanogr. **50**: 1771–1786.

Tryon, M. D., K. M. Brown, and M. E. Torres. 2002. Fluid and chemical fluxes in and out of sediments hosting methane hydrate deposits on Hydrate Ridge, OR, II: Hydrological provinces. Earth Planet. Sci. Lett. **201**: 541–557.

Tryon, M. D., C. G. Wheat, and D. R. Hilton. 2010. Fluid sources and pathways of the Costa Rica erosional convergent margin. Geochemistry, Geophys. Geosystems **11**: n/a–n/a.

908 Visser, W., W. A. Scheffers, W. H. Batenburg-van der Vegte, and J. P. van Dijken. 1990. Oxygen
909 requirements of yeasts. Appl. Environ. Microbiol. **56**: 3785–3792.

910 Wallmann, K., M. Drews, G. Aliosi, G. Bohrmann. 2006. Methane discharge into the Black Sea and the
911 global ocean via fluid flow through submarine mud volcanoes. Earth Plan. Sci. Let. **248:** 545-560.

912 Wallmann, K., E. Pinero, E. Burwicz, M. Haeckel, C. Hensen, A. Dale, and L. Ruepke. 2012. The Global
913 Inventory of Methane Hydrate in Marine Sediments: A Theoretical Approach. Energies **5**: 2449–
914 2498.

915 Wankel, S. D., M. M. Adams, D. T. Johnston, C. M. Hansel, S. B. Joye, and P. R. Girguis. 2012.
916 Anaerobic methane oxidation in metalliferous hydrothermal sediments: influence on carbon
917 flux and decoupling from sulfate reduction. Environ. Microbiol. **14**: 2726–40.

918 Whiticar, M. J. 2002. Diagenetic relationships of methanogenesis , nutrients, acoustic turbidity ,
919 pockmarks and freshwater seepages in Eckernförde Bay. Mar. Geol. **182**: 29–53.

920 Widdel, F., and F. Bak. 2006. Gram-negative mesophilic sulfate-reducing bacteria, p. 3352–3378. *In*
921 M. Dworkin, S. Falkow, E. Rosenberg, K.-H. Schleifer, and E. Stackebrandt [eds.], The
922 Prokaryotes. Springer US.

923 Wyrtki, K. 1962. The oxygen minima in relation to ocean circulation. Deep. Res. **9**: 11–23.

924

Figure Captions:

Figure 1: Depth profiles of measured and modeled porewater parameters and microbial turnover rates for SO206-29 (MUC), sampled from 402 m water depth. A) measured (diamonds) and modeled (thick green line) sulfate concentrations (per L porewater), as well as measured (circles) and modeled (thick blue line) methane concentrations (per L sediment), (B) three replicates (thin lines and symbols) of measured sulfate reduction rates (per cm^{-3} sediment), C) three replicates of measured (thin lines and symbols) and modeled (thick line) AOM rates (per cm^{-3} sediment), D) measured (triangles) and modeled sulfide concentration (thick orange line), measured (squares) and modeled (thick grey line) total alkalinity (per L porewater).

Figure 2: Depth profiles of measured and modeled porewater parameters and microbial turnover rates for SO206-31 (MUC) sampled from 401 m water depth. Thick solid lines = pw-fit model, thick dashed lines = hf-fit model (for details see Results). A) measured (diamonds) and modeled (thick green lines) sulfate concentrations (per L porewater), measured (circles) and modeled (thick blue lines) methane concentrations (per L sediment), B) three replicates (thin lines and symbols) of measured sulfate reduction rates (per cm^{-3} sediment), C) three replicates of measured (thin lines and symbols) and modeled (thick lines) AOM rates (per cm^{-3} sediment), D) measured (triangles) and modeled (thick orange lines) sulfide concentration, measured (squares) and modeled (thick grey lines) total alkalinity (per L porewater).

Figure 3: Sulfate and bromide concentrations (left panel), sulfide and total alkalinity concentrations (middle panel), redox potential and pH (right panel) measured in the sediment of the low flow regime core (LFC) from Quepos Slide after different days of runtime indicated on the left. All concentrations are presented per L porewater. Please consider the different scales for sulfide concentrations.

951 Figure 4: Sulfate and bromide concentrations (left panel), sulfide and total alkalinity concentrations
952 (middle panel), redox potential and pH (right panel) measured in the sediment of the high flow
953 regime core (HFC) from Quepos Slide after days of runtime indicated on the left. The SBTZ as proxy
954 for the SMTZ is highlighted by the grey bar. All concentrations are presented per L porewater. Please
955 consider the different scales for sulfide concentrations.
956
957 Figure 5: Methane concentration (µmol l^{-1}) in the outflow (A, D), methane efflux (mmol m^{-2} d^{-1}; B, E),
958 and calculated AOM rate (mmol m^{-2} d^{-1}; C, F) of the SLOT system before and after changing the fluid
959 flow regime: (A, **B,** C) low flow regime core (LFC), and (D, E, F) high flow regime core (HFC) from
960 Quepos Slide. Vertical lines mark the moment of fluid flow change (low flow → high flow and vice
961 versa at 258 d runtime). Error bars (A, D) show standard deviations of three repeated gas
962 chromatographic measurements; the first two data points represent single measurements. Dotted
963 lines represent the trendline (low flow regime: $5x10^{-6} * t_{runtime}^2 + 0.02\ t_{runtime} + 0.285$, $r^2 = 0.825$; high
964 flow regime: $0.8576 * \ln(t_{runtime}) - 0.8662$, $r^2 = 0.987$) of methane concentration development until
965 flow change.
966
967 Figure 6: Solute concentrations and turnover rates in the new high flow core (NHFC) after experiment
968 termination (358 d runtime). Porewater profiles of methane (A, crosses), sulfate (B, crosses), sulfide
969 (C, circles), and results of the radiotracer measurements for AOM (A, bars) and sulfate reduction (B,
970 bars) are shown.
971
972 Figure 7: Solute concentrations and turnover rates in the new low flow core (NLFC) after experiment
973 termination (358 d runtime). Porewater profiles of methane (A, crosses), sulfate (B, crosses), sulfide
974 (C, circles), and results of the radiotracer measurements for AOM (A, bars) and sulfate reduction (B,
975 bars) are shown.
976

977 Figure 8: Sediment solid phase parameters measured in the sediment of the ex situ replicate SO206-
978 31 (MUC) core (grey lines and symbols) compared to the NHFC (original LFC, black lines and symbols).
979 Total carbon content (TC, diamonds), and total inorganic carbon content (TIC, circles) in dry wt.% (A);
980 atomic C/N ratio (circle) and total organic carbon content (TOC, triangles) in dry wt.% (B); total
981 nitrogen (TN, diamonds), total sulfur (TS, circles) in dry wt.% (C); porosity of the sediment (D).
982

983 Figure 9: Sediment solid phase parameters measured in the sediment of the ex situ replicate of the
984 SO206-31 (MUC) core (grey lines and symbols) compared to the NLFC (original HFC, black lines and
985 symbols). Total carbon content (TC, diamonds), and total inorganic carbon content (TIC, circle) in dry
986 wt.% (A); atomic C/N ratio (circle) and total organic carbon content (TOC, triangles) in dry wt.% (B);
987 total nitrogen (TN, diamonds), total sulfur (TS, circles) in dry wt.% (C); porosity of the sediment (D).
988

989

990

Tables:

Table 1: Sampling sites of the Quepos Slide and the SMTZ depth in cm below seafloor (bsf).

Station	Latitude (N)	Longitude (W)	Water depth m	Depth of SMTZ cmbsf
SO206-29 (MUC)	8°51.29'	84°12.60'	402	12.5 - 22.5
SO206-31 (MUC)	8°51.12'	84°13.06'	399	5.0 - 15.0

995 Table 2: Summary of input parameters used for the model simulations and major model results. For
996 the SO206-31 (MUC) cores, two fits are provided, since the replicate core for porewater
997 determinations (pw-fit) exhibited a lower fluid flow and deeper SMTZ than the core used for rate
998 deteminations (hf-fit), probably as a result of high fluid flow heterogeneity at the site (see
999 discussion). For more model details, see Krause et al. 2014.

Parameter	SO206-29 (MUC)	SO206-31 (MUC) pw-fit	SO206-31 (MUC) hf-fit	Unit	Parameter source
Model parameter values					
Length core	32	44	44	cm	measured
Length of simulated column	80	80	50	cm	fitted
Number of model layers	160	200	200		set
Temperature	8	8	8	°C	measured
Salinity	35	35	35	PSU	measured
Pressure	41	41	41	bar	measured
Porosity at sediment surface	0.95	0.93	0.93		measured
Porosity at the base of the sediment core	0.75	0.70	0.70		measured
Porosity at infinity sediment depth	0.74	0.70	0.70		fitted
Attenuation coef. for porosity decrase with depth	0.04	0.04	0.04	cm^{-1}	fitted
Burial velocity at depth	0.02	0.02	0.03	cm yr^{-1}	fitted
Fluid flow at the sediment water interface	7	5	29	cm yr^{-1}	fitted
Kinetic for AOM	200000	25000	100000	cm $mmol^{-1}$ yr^{-1}	fitted
Kinetic constant for $CaCO_3$ precipitation	0	0	0	yr^{-1}	fitted
Density of dry solids in sediment	2.5	2.5	2.5	g cm^{-3}	assumed
Kinetic constant for TH_2S removal from porewater	0.02	0.1	0.005	mmol cm^{-3} yr^{-1}	fitted
Attenuation coef. for decrease in TH_2S removal rate	0.07	0.6	0.05	cm^{-1}	fitted
Non-local mixing coefficient	1.5	0	80	yr^{-1}	fitted
Depth of irrigated layer	15	0	2	cm	fitted
Width of irrigated layer	5	0	1.5	cm	fitted
Porewater concentration upper/lower boundary					
Bottom water / Bottom sediment SO_4^{2-}	28.00 / 0.00	27.00 / 0.00	27.00 / 0.00	mmol l^{-1}	measured
Bottom water / Bottom sediment CH_4	0.00 / 61.00	0.00 / 61.00	0.00 / 61.00	mmol l^{-1}	calculated*
Bottom water / Bottom sediment Cl^-	558.00 / 380.00	548.00 / 320.00	548.00 / 320.00	mmol l^{-1}	measured
Bottom water / Bottom sediment HCO_3^-	2.30 / 10.00	4.00 / 15.00	4.00 / 15.00	mmol l^{-1}	measured
Bottom water / Bottom sediment TH_2S	0.00 / 0.00	0.03 / 0.00	0.03 / 0.00	mmol l^{-1}	measured
Model Results					
Methane flux at sediment bottom	12.40	9.09	45.09	mmol m^{-2} d^{-1}	modeled
Methane efflux at sediment water interface	0.98	0.00	3.39	mmol m^{-2} d^{-1}	modeled
Percentage of consumed methane	91.53	100.00	92.46	%	modeled
Anaerobic oxdation of methane	11.35	9.09	41.69	mmol m^{-2} d^{-1}	modeled
Measured turnover rates (radiotracer techniques)					
Sulfate reduction (entire sediment depth)	13.38 ± 13.61	218.90 ± 159.80	218.90 ± 159.80	mmol m^{-2} d^{-1}	measured
AOM (entire sediment depth)	12.87 ± 5.98	45.15 ± 11.48	45.15 ± 11.48	mmol m^{-2} d^{-1}	measured

*Calculated after Tishchenko et al. 2005

1000

1001

1002

1003 Table 3: Salt concentrations of the two different media used in the SLOT-system. Seawater medium

1004 with sulfate was delivered from the top, seepage medium with methane and without sulfate from

1005 the bottom. In the last line, the gas in the respective medium headspace is denoted.

Salts (all in mmol l^{-1})	**Seawater medium (with SO_4^{2-})**	**Seepage medium (with CH_4)***
KBr	0.006	0.756
KCl	8.05	8.05
$CaCl_2$ $2H_2O$	10.0	10.0
$MgCl_2$ $6H_2O$	27.9	55.5
$MgSO_2$ $7H_2O$	27.6	0.000
NaCl	451	451
Medium headspace	N_2	CH_4

* $FeSO_4$ (trace element) was replaced by FeCl (compare Widdel and Bak 2006)

1006

1007

1008

1009 Table 4: Overview of conditions during SLOT experiments: methane concentration of the "seepage"
1010 medium, methane flux, advective flow, and pump rate in the low and high flow core as well as
1011 experimental phases and run times under the low and high flow regime. The length of the sediment
1012 cores was 15 (LFC) and 14 (HFC) cm.

	low flow regime	**high flow regime**
Methane in µmol l^{-1} (seepage medium)	965 ± 180	
Methane flux* in mmol m^{-2} d^{-1}	0.28	2.81
Advective flow in cm yr^{-1}	10.6	106.3
Pumping rate µl min^{-1} (seepage medium)	0.5	5
Hydrological Residence Time (HRT)	1080	108
Experimental phase	**total time**	**phase time**
Initial	-40 - 0	40
Phase 1	0 - 258	258
Phase 2	258 - 350	92

*Calculated by the methane concentration of the seepage medium multiplied by the advectiv flow

1013

1014

1015 Table 5: Fluid flow, methane emissions, methane fluxes, and AOM rates determined in sediments

1016 from cold seep sites covered with sulfur bacteria mats.

Cold seep sites with bacterial mats	Water depth (m)	Fluid flow (cm yr^{-1})	Methane emission (mmol m^{-2} d^{-1})	Methane flux from depth (mmol m^{-2} d^{-1})	Depth integrated AOM rate (mmol m^{-2} d^{-1}) Max rate (nmol cm^{-3} d^{-1})	Source
Quepos Slide						This study
SO206-29 (MUC)	402	7*	0.98*	12.4*	12.87 (0-32 cm)/11.35* (0-80 cm)	
SO206-31 (MUC) pw	399	5*	0.00*	9.09*	45.15 (0-44 cm)/9.09* (0-80 cm)	
SO206-31 (MUC) hf	399	29*	3.39*	45.09*	45.14 (0-44 cm)/41.69* (0-50 cm)	
LFC/NHFC	399	10.6	0.011-0.030/0.165	0.28	0.304[+]/2.970 (0-15 cm)[+]	
HFC/NLFC	399	106.3	0.025-0.109/0.009	2.81	3.114/0.306 (0-14 cm)	
Quepos Slide						Karaca et al. 2010
TV-MUC-63	406	40*	52.5*		58.4* (0-41.5 cm)	
TV-MUC-73	404	4*	20.2*		22.2* (0-32.5 cm)	
Mound 11	1024	200*/300*[1]	318.5*		9.6* (0-27.5 cm)	Hensen et al. 2004
Culebra Fault	1530	0.1*	0*		0.4* (0-810 cm)	
Pockmark	1917	3*	5.2*		9.2* (0-15 cm)	
Quepos Slide	397-410	1-40*	0.2-56.1*		1.5-42.1*	Karaca et al. 2012
Mound 12	1000	10*	0.01-3.8[#]/12.1*	28.3* (10 cm)	16.1* (0-10 cm)	Linke et al. 2005
Mound 12	1000	10	12.1-89.9		4.9-140.0	Mau et al. 2006
Mound 11						Krause et al. 2014
SO206-39	1005	200*	201.63*		140.71 (0-10 cm)/143.69* (0-100 cm)	
SO206-50	1003		0.30*		4.76 (0-270 cm)/1.62* (0-500 cm)	
Mound 12						
SO206-44	1007	15*	4.28*		22.37 (0-10 cm)/22.23* (0-100 cm)	
SO206-46	1009		12.45*		10.68 (0-10 cm)/16.16* (0-100 cm)	
Green Canyon C4324	560				11.6 (0-13.5 cm) Max: 500 (13.5 cm)	Joye et al. 2004
(Gulf of Mexico) C4315	540				4.61 (0-10.5 cm)	
Hydrate Ridge	777	10-250	30-100[#]			Torres et al. 2002
(NE Pacific)	777		0.6-4*		99.0 (0-10 cm) Max: 5500 (8-9 cm)	Treude et al. 2003
	778	20*	5.7[#]	16.5* (20 cm)	15.1*	Sommer et al. 2006
Håkon Mosby mud volcano	1250	250			0.55 (0-80 cm) Max: 0.8 (20-30 cm)	Pimenov et al. 1999
					6.7 (0-20 cm)	Lein et al. 1999
(North Atlantic)		30-60			12.32 (0-10 cm)	Niemann et al. 2006
Kazan mud volcano (Mediterranean Sea)	2000	3-5	0*	130 mM at depth		Haese et al. 2003
Dvurechenskii mud volcano (Black Sea)	2070	8-25*	3.4-11.1*	21.6-58.3*	16.7 (0-18 cm)/18.2-47.2* (0-26/38cm) Max: 563 (1 cm)	Wallmann et al. 2006

1017 *Model result, [#]benthic chamber/barrel measurement, [+]rate most likely overestimated as no steady state was reached.

Figures:

Figure 1:

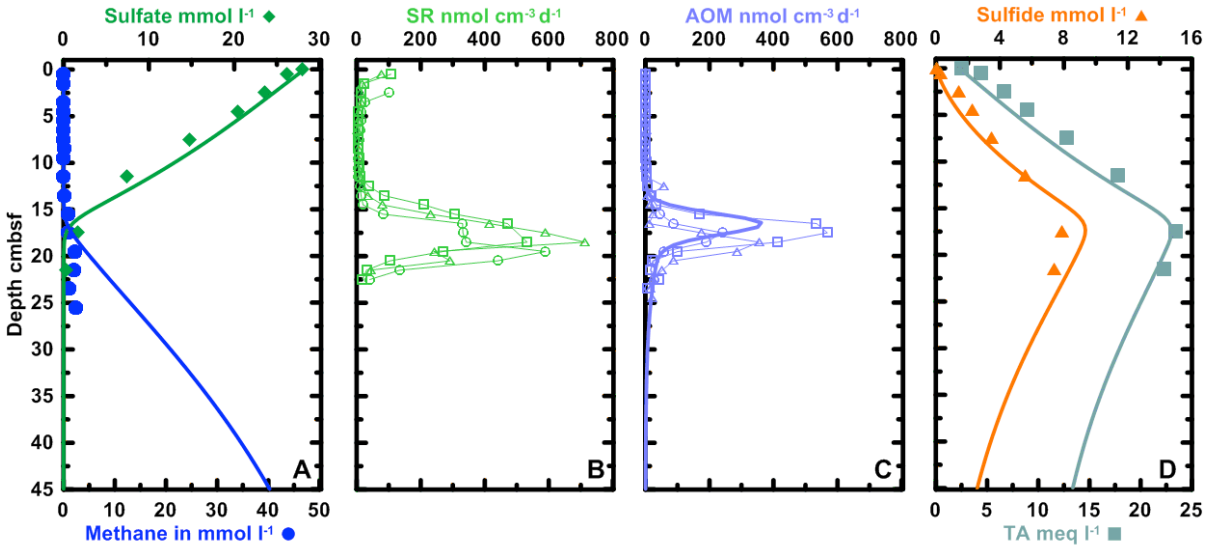

1023 **Figure 2**

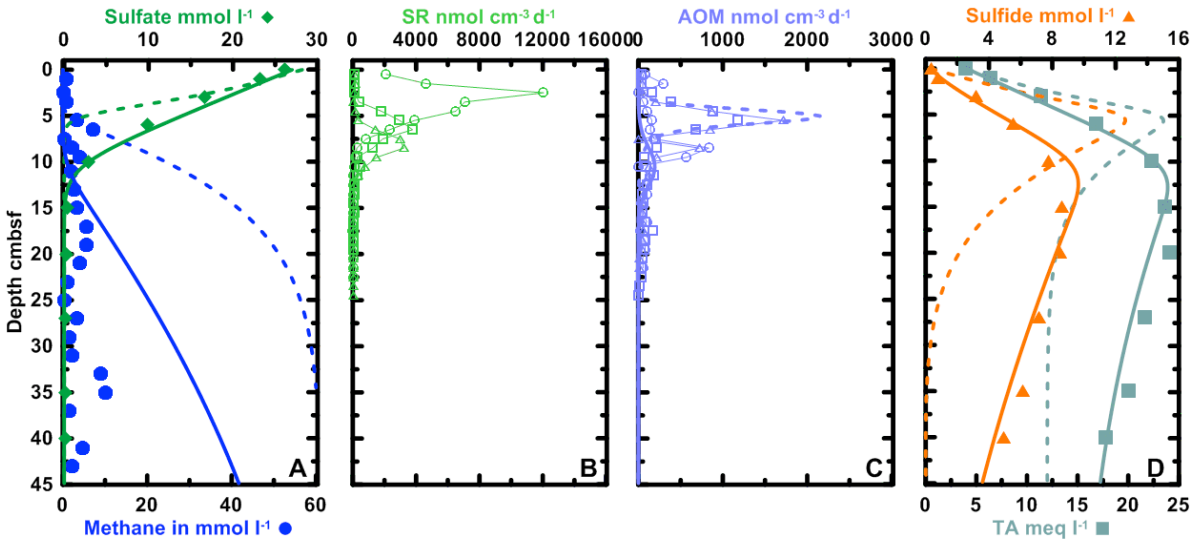

1024

1025

1026

1027

Figure 3

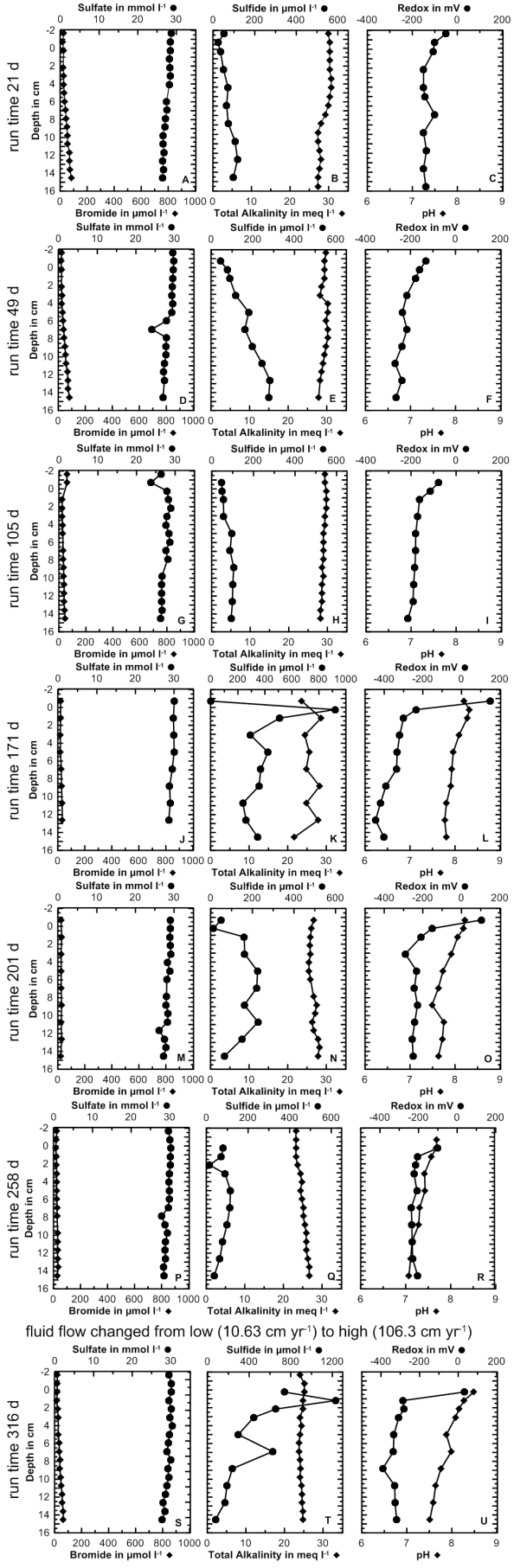

fluid flow changed from low (10.63 cm yr^{-1}) to high (106.3 cm yr^{-1})

1028

1029

Figure 4

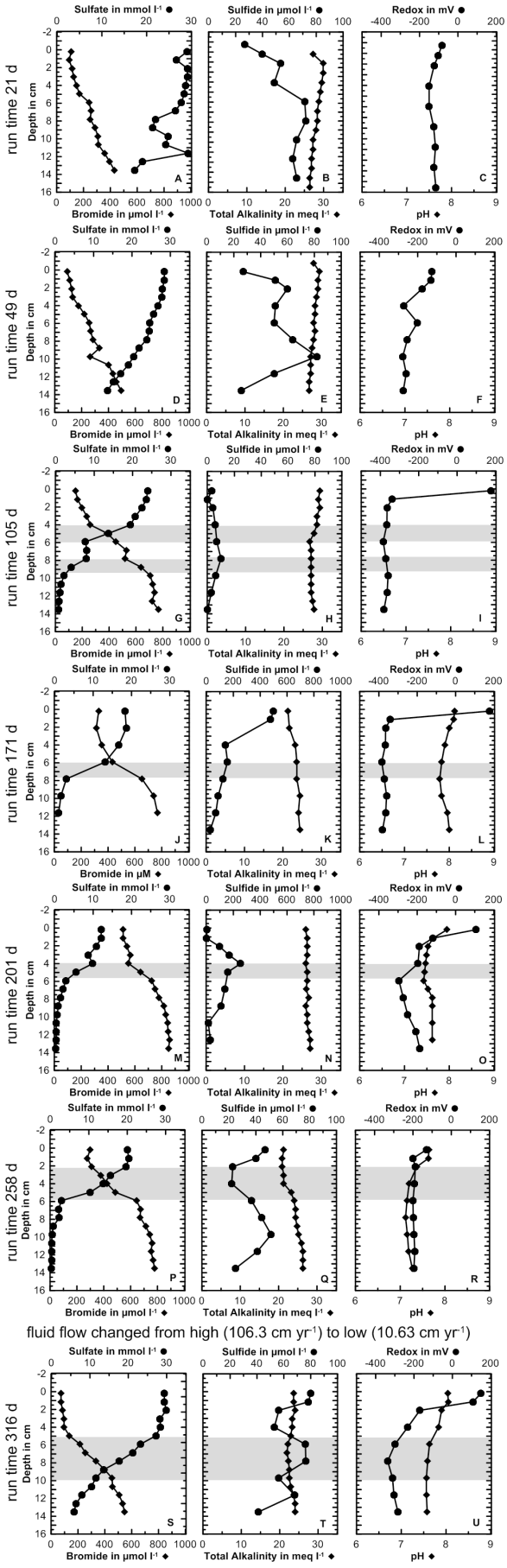

fluid flow changed from high (106.3 cm yr^{-1}) to low (10.63 cm yr^{-1})

1030

Figure 5

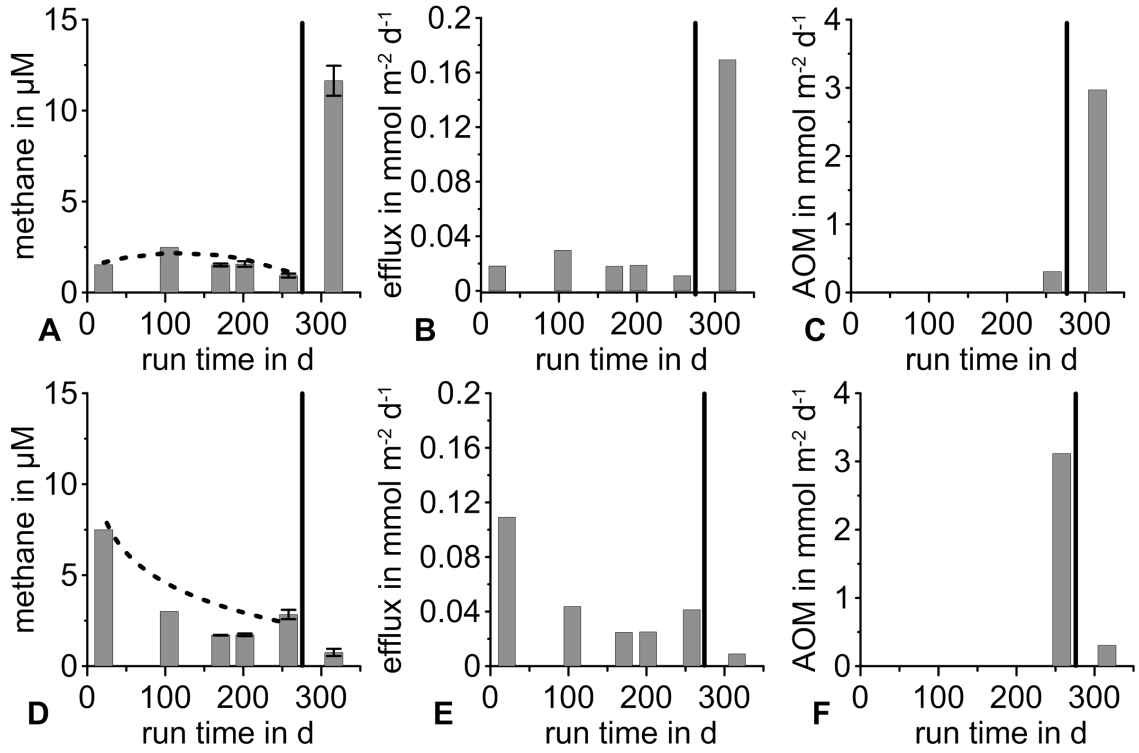
methane in µM
efflux in mmol m-2 d-1
AOM in mmol m-2 d-1
run time in d
A
B
C
D
E
F

1035 **Figure 6**

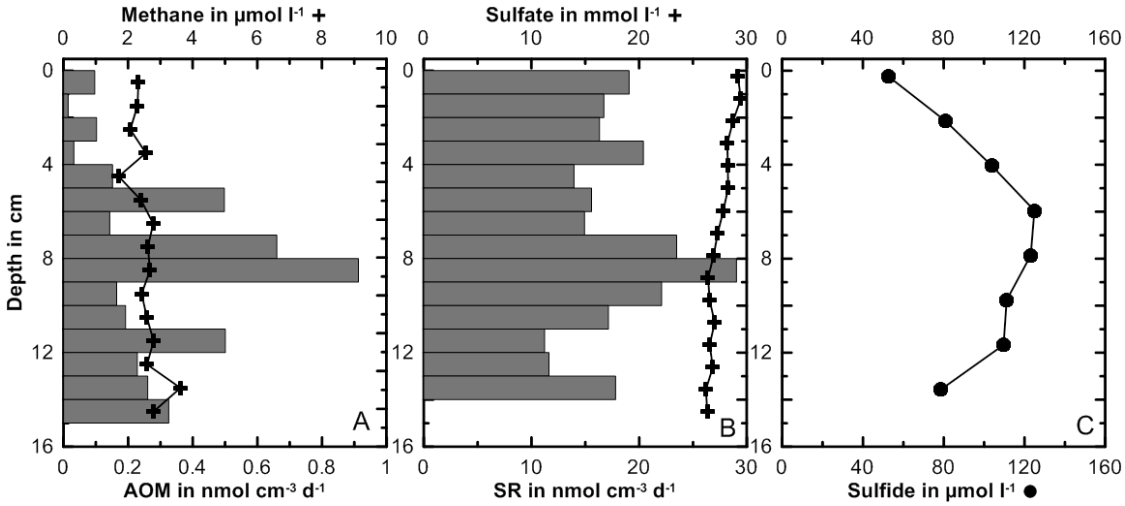

1036

1037

1038 **Figure 7**

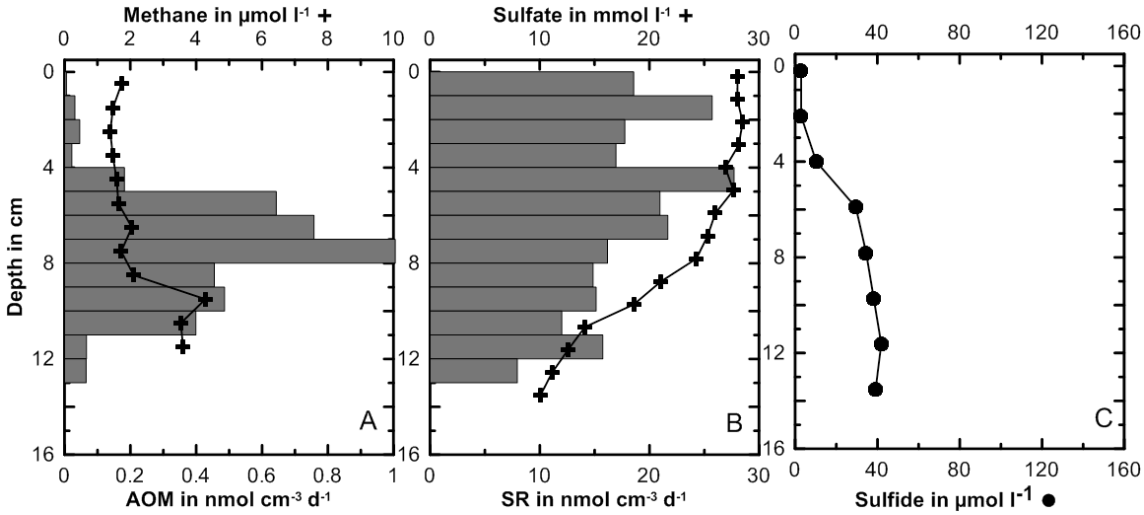

1039

1040

1041

Figure 8

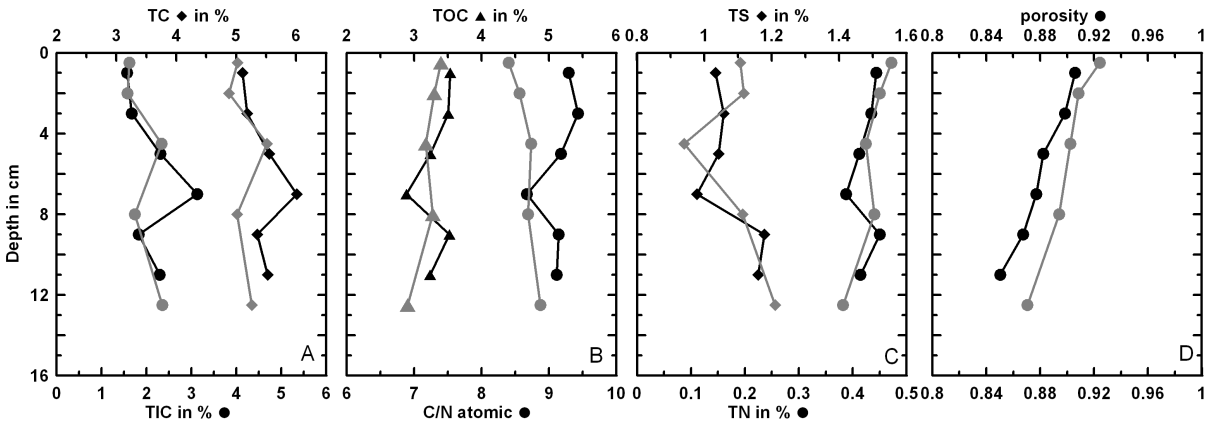

1042

1043

1044

Figure 9

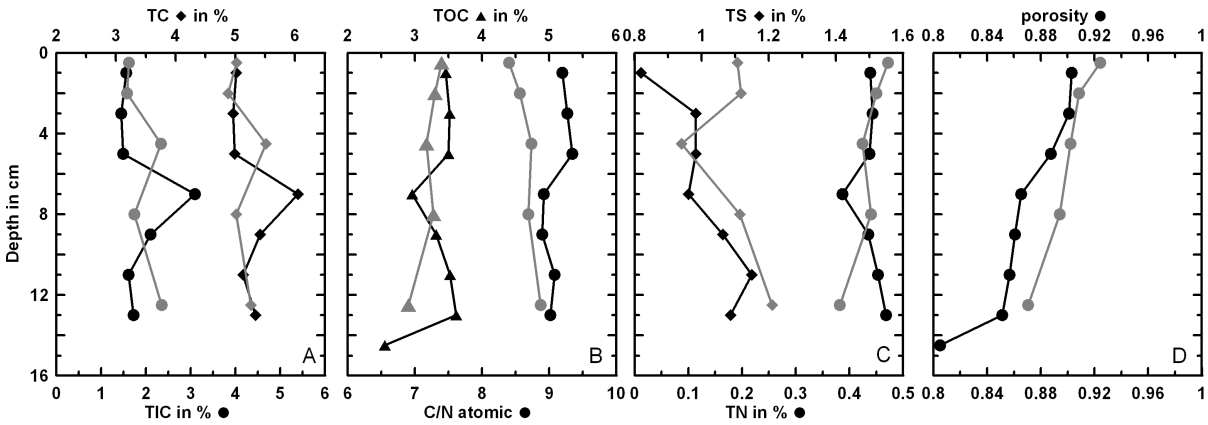

1045